Focussing of light inside turbid media

Eibert G. van Putten

Graduation Thesis
Master of Science, Applied Physics
September 21, 2007

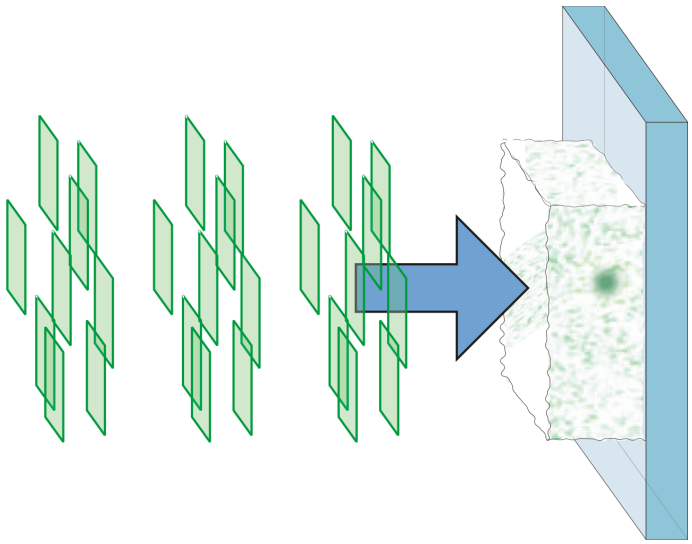

Focussing of light inside turbid media

Master's thesis
Master of Science, Applied Physics
Eibert G. van Putten
September 21, 2007

Graduation committee:
Ir. I.M. Vellekoop (COPS)
Dr. A.P. Mosk (COPS)
Prof. dr. A. Lagendijk (COPS and AMOLF)
Dr. ir. A. Brinkman (Low Temperature Division)

This work was done at COPS:
Complex Photonic Systems
MESA$^+$ Institute for Nanotechnology
Faculty of Science and Technology
University of Twente
P.O. Box 217
7500 AE Enschede

Nature does nothing uselessly

Aristotle (384 BC - 322 BC)

Acknowledgements

In the last nine months I had the opportunity to work on an exciting project in the Complex Photonic Systems (COPS) group. I enjoyed being part of this group of motivated, talented, and inspiring people. The scientific discussions, the enthusiasm of many people, and critical attitude of the group created a pleasant working atmosphere in which I learned a lot.

Ivo Vellekoop and Allard Mosk took the daily supervision of this project on them. Ivo, I want to thank you for you excellent guidance. No question was too much. You always found some time to help me understand many theoretical and practical problems. Allard, every day again you amaze me with the extraordinary amount of knowledge you carry with you. Your enthusiasm and insight in physics worked very catching. I like to thank Ad Lagendijk for many inspiring discussions. Every time I visited AMOLF, I walked out of his office full of new and interesting ideas. Ad, I also like to thank you for being the chairman of my graduation committee.

I thank all the members of the COPS group and the group of Photonic Bandgaps at AMOLF; Philip, Leon, Charles, Willem T., Karen, Bart, Alex, Steven, Merel, Paolo, Bernard, Tom, Patrick, Pedro, Otto, Sanli, Ramy, Frerik, Edwin and Niels. I would like to thank Willem Vos for his excellent guidance of the COPS group and his interesting discussions during the weekly group meetings. I am grateful to Willem Tjerkstra for careful reading an early draft of my thesis. Cock, thank you for your help in the optical lab. I thank Bas for his technical ICT support, Karen for her administrative support, and Raymond for cheering up our office with his many political incorrect jokes. I would like to thank Alexander Brinkman from the Low Temperatures Division for looking at my work from a different point of view and for being part of my graduation committee.

My family has always supported me during my study. I thank my parents, my brother, and my sister for their care. Vera, you are my definition of true love. Thank you for your support, your love, and for your patience.

Elbert van Putten
Enschede, September 2007

Abstract

Turbid media are opaque because of multiple scattering of light. Inhomogeneities on the length scale of the wavelength scatter the light and prevent a straight propagation through the media. Complex multiple wave interference creates a random granular intensity pattern inside and outside the scattering material. When the material is disordered, it is impossible to predict the form of the complex interference pattern. We demonstrate experimentally a novel method to focus light at any desired position deeply inside strongly scattering materials. A fluorescent microsphere is positioned inside the scattering material to act as a probe for the local intensity of the excitation light. The fluorescent emission is used to construct a specific linear combination of incident waves. This special combination of waves scatter multiple times and interfere constructively exactly at the position of the probe, creating an intense focus deeply inside the medium. Our approach provides a fundamentally new way of controlling light in turbid media.

Contents

List of Abbreviations and Symbols

CCD	Charge-coupled device (camera)
d_a	Normalized inner product of G_{ba} with the present background field
D	Diffusion constant
EMCCD	Electron multiplying charge-coupled device (camera)
E_a	Field of incoming scattering channel a
E_b	Field at position $\mathbf{r}_b$
E_{sp}	Electric field of a super pixel
g	Bare Green's function
G	Full Green's function
G_{ba}	Complex field coefficient from channel a to position $\mathbf{r}_b$
I	Intensity
I_b	$\lvert E_b\rvert^2$
I_{ex}	Intensity of the excitation light
I_{fl}	Fluorescence intensity
I_{ref}	Speckle averaged fluorescence intensity
I_{scan}	Highest fluorescence intensity achieved by scanning the sample
$\mathbf{J}$	Flux
n	Refractive index
N	Number of (controlled) incident scattering channels
M	Number of detected modes
k	Wave vector
K	Effective wave vector
ℓ_{tr}	Transport mean free path
L	Sample thickness
P_α	Probability density function of α
V	Scattering potential
R	Ensemble averaged intensity propagator
SLM	Spatial light modulator
T	Total transmission
TN LCD	Twisted nematic liquid crystal display

z_e	Extrapolation length
ZnO	Zinc Oxide
η	Theoretical maximal intensity enhancement
η_{opt}	Intensity enhancement by channel demixing
η_{scan}	Intensity enhancement by scanning the sample
ϕ_a	Phase of incoming scattering channel a
ϕ_{ba}	Phase of field coefficient G_{ba}
Ψ	Complex field amplitude
$\langle\cdot\rangle$	Ensemble average operator

List of Figures

CHAPTER 1

Introduction

1.1 Light and matter

Light and matter can interact with each other in various ways; matter can for example absorb, emit or scatter light. If we look around us, nature gives us many wonderful examples of these different types of interactions. Most plants are green because their leafs absorb light, mainly in the red and the blue, to fuel their photosynthesis, while the red-orange color of lava is due to light emission by the hot molten rock. The beautiful colors of a rainbow, the breathtaking sparkling of diamonds, and the blue sky are all manifestations of light scattering.

In many materials of medical relevance, light is scattered rather than absorbed or emitted. Examples are turbid media such as teeth, bone and soft biological tissue. Imaging of these materials is troublesome; light propagating through turbid materials experiences multiple scattering and becomes diffusive, hiding the intrinsic structures from the outside world.

1.2 Turbid media

In a homogeneous world, light propagates as a ray; along a straight light with a constant speed. The air around us behaves in many ways like a homogeneous medium. Light scattered from or emitted by an object can propagate in a straight line through air. On a clear day, we can easily discriminate objects that are hundreds of meters away because the light is able to reach our eyes undisturbed.

Turbid media are the opposite of homogeneous media; a dense concentration of particles causes random inhomogeneities that scatter and prevent a straight propagation of light. Multiple scattering of light distort an incident wavefront so strongly that all spatial

coherence is lost. An object placed behind or inside a turbid medium is no longer discernible because scattering blurs and distorts the image. Walking outside on a foggy day clearly illustrates how multiple light scattering limits the ability to discriminate objects from their surroundings. The random scattering of light makes a turbid medium opaque.

In the same way that light from inside a turbid media cannot freely exit the medium, we cannot simple concentrate light onto an object that is located inside a turbid material. Multiple scattering of light prevents direct focussing of light inside an opaque medium. Light diffuses, spreading the intensity instead of concentrating it onto one point.

Control over the propagation of light inside turbid media is important for many different applications. In biomedical imaging, efficient light delivery could increase the contrast of techniques like optical coherence tomography [1], time gated techniques [2–4], and fluorescence microscopy [5]. A different application would be to selectively activate photochemical processes by concentrating light at a point inside a scattering material. Although the high relevance of controlling light inside turbid media, nobody has ever demonstrated focussing of light deeply inside turbid media.

1.3 Focussing light inside turbid media

In this thesis we present a technique to effectively bring light to fluorescent objects embedded deeply inside turbid media. The technique we use, was recently developed by Vellekoop and Mosk [6] to focus light through a strongly scattering sample. We use the same technique to focus light inside turbid media. Our experiment works as follows. We consider a scattering sample with embedded fluorescent spheres. As soon as we illuminate the turbid sample with coherent light, a granular intensity pattern arises. This pattern is caused by alternating constructive and destructive interference of light traveling along different paths in the medium. The light is scattered multiple times and arrives with different phases at the spheres inside the sample. The relative phases between the different path contributions determine whether the interference is constructive or destructive. Under standard illumination, the phases of the independent contributions will be random and unrelated to each other. There is no position inside the sample where all the path contributions are exactly in phase.

The fluorescent spheres inside our sample emit light, proportional to the local intensity of the excitation light. If we want to bring light to a certain target sphere, all the path contributions need to interfere constructively at the position of this sphere. We gain control over the independent path contributions using a spatial light modulator (SLM). With this SLM we can synthesize wavefronts of any desired shape. We find the relative phases of each field contribution by modulating them, one after the other, while monitoring the fluorescent emission of the sphere. From these measurements we are able to deduce the optimal wavefront that interferes constructively on a single sphere hidden inside the turbid sample. This local constructive interference creates a focus with a size in the order of $\lambda/2$. The excitation light also determines the limiting depth that can be reached with this technique. The diffusive path length to the target should be smaller than the coherence length of the excitation light, making it possible to deliver light centimeters deep inside even in the strongest scattering samples.

1.4 Overview of the thesis

In Chapter 2 we discuss the behavior of light inside a random medium. We focus on the diffusion equation. We solve this equation for a slab geometry, which is a good approach of the sample geometry used in our experiments. Furthermore we look at the intensity distribution of multiple scattered light and describe the light scattering as a mixing of scattering channels. This channel mixing can be reversed, a process we define as channel demixing. We explain the principles of channel demixing and deduce the maximal expected intensity at the formed focus.

In Chapter 3 the experimental apparatus, used in the channel demixing experiments, is described. The apparatus consist of a part that handles the light delivery and detection, and a part that is able to shape the wavefronts of a light beam. The wavefront shaping part of the apparatus uses a novel technique which solves existing cross-modulation problems in spatial light modulators. This novel technique is described in detail. The algorithm used to form the optimal wavefront is also described in chapter 3.

In Chapter 4 we describe the samples used in this project. Strongly scattering samples of zinc oxide, doped with fluorescent spheres were fabricated in two different forms; one type of samples has the fluorescent spheres dispersed in a layer of zinc oxide, while the other type has the fluorescent spheres under the zinc oxide layer. In this chapter we discuss the fabrication and characterization.

In Chapter 5 we present the results of our channel demixing experiments. In these experiments we focussed light onto targets at different depths inside the opaque samples.We address the analysis of the data and discuss the different experimental aspects that were needed to determine the achieved intensity enhancements. A comparison is made between standard scanning illumination and the channel demixing technique. Furthermore we present the results of different characterization experiments.

CHAPTER 2

Theory

2.1 Introduction

In this chapter the behavior of light inside random media is studied. Light propagating through random media is scattered multiple times and diffuses through the medium. Diffusion of light is treated using a theoretical framework based on Green's functions and multiple scattering. This multiple scattering theory is not new and a detailed description can be found at many places in literature (see for example [7–11]). We follow the approach and the notation used by Vellekoop [10]. In section 2.2 we introduce the diffusion equation. In section 2.3 we then apply the diffusion equation to a slab geometry.

Diffusion of coherent light is only seen when the intensity is ensemble averaged. When a single instance is considered, the intensity will spatially fluctuate due to interference. This granular intensity pattern is usually called a speckle pattern. The average size of a speckle is used to define small correlation areas that are called scattering channels. Light entering the scattering sample through different channels is mixed thoroughly, leading to the spatially alternating destructive and constructive interference. In section 2.4 the statistical intensity distribution of multiple scattered light is derived.

In a scattering medium, the light is mixed and spread out through the sample. By controlling the way the light enters the medium, it is possible to influence the propagation of light and even focus it on any desired position. Sending in a specially shaped wavefront, we can make the light interfere constructively at a desired position deeply inside the scattering medium. In section 2.5 we explain how we find the right wavefront to focus light inside the medium, we discuss the expected intensity increase at the focus and we derive an equation for the intensity enhancement when light is optimized to focus at multiple independent detectors at the same time.

2.2 Behavior of light inside random media

To describe the behavior of light inside random media we will first discuss the propagation of the electric field in a homogenous medium. A corresponding Green's function will be derived. Using the Green's function for a homogenous medium, we derive a Green's function describing the field propagation in an inhomogeneous medium. From the field propagator, we find an approximate expression for the intensity propagator which eventually leads to the diffusion equation.

2.2.1 The field propagator in homogeneous media

The propagation of light is well described by Maxwell's equations. The electric and the magnetic field are vector quantities, but unfortunately the vector description of light inside random media is very complicated. If polarization effects are negligible we can model propagation of light by treating light as a scalar quantity. From the Maxwell equations we find the scalar wave equation:

$$\nabla^2\Psi(\mathbf{r},t) - \frac{n^2}{c^2}\frac{\partial^2}{\partial t^2}\Psi(\mathbf{r},t) = 0, \tag{2.1}$$

with Ψ the complex amplitude of the electric field, n the refractive index of the medium and c the speed of light in vacuum. In a homogeneous medium the refractive index does not depend on the position. Fourier transforming Eq. 2.1 with respect to time gives the scalar Helmholtz wave equation

$$-\nabla^2\Psi(\mathbf{r},\omega) - k^2\Psi(\mathbf{r},\omega) = 0, \tag{2.2}$$

where $k \equiv n\omega/c$ with ω the angular frequency of the light.

To solve Eq. 2.2 we introduce the Green's function. The Green's function is the solution to the wave equation in the presence of a point source at position r'. Because the Green's function describes the propagation of light it is also called the propagator. For a homogeneous medium we find the bare Green's function g, by solving

$$-\nabla^2 g(\mathbf{r},\mathbf{r}',\omega) - k^2 g(\mathbf{r},\mathbf{r}',\omega) = \delta(\mathbf{r}-\mathbf{r}'), \tag{2.3}$$

where $\delta(\mathbf{r}-\mathbf{r}')$ is the Dirac δ-function. The bare Green's function is found to be [10]:

$$g(\tilde{\mathbf{r}},\omega) = -\frac{e^{ik(\omega)\tilde{r}}}{4\pi\tilde{r}}, \tag{2.4}$$

a spherical wave with a spatial frequency k propagating away from the origin. The bare Green's function only depends on the difference between $\mathbf{r}$ and $\mathbf{r}'$ which allows us to write g as a function of $\tilde{\mathbf{r}} \equiv \mathbf{r}-\mathbf{r}'$.

2.2.2 The field propagator in inhomogeneous media

For an inhomogeneous medium, the refractive index is a function of the position, following the irregularities in the medium. We write the refractive index as $n(\mathbf{r}) \equiv \sqrt{n_0^2 + \Delta n^2(\mathbf{r})}$

with n_0 the constant refractive index of the background. The time independent wave equation inside an inhomogeneous medium reads:

$$-\nabla^2\Psi(\mathbf{r},\omega) - k^2(\omega)\Psi(\mathbf{r},\omega) = V(\mathbf{r},\omega)\Psi(\mathbf{r},\omega), \tag{2.5}$$

with $V(\mathbf{r},\omega) \equiv \Delta n^2(\mathbf{r})\frac{\omega^2}{c^2}$ the position dependent scattering potential. We can now find a new Green's function that describes the propagation from $\mathbf{r}'$ to $\mathbf{r}$ in the inhomogeneous medium [10]. This Green's function is called the full Green's function G,

$$G(\mathbf{r},\mathbf{r}',\omega) = g(\mathbf{r}-\mathbf{r}',\omega) + \int d\mathbf{r_1} g(\mathbf{r}-\mathbf{r}_1,\omega)V(\mathbf{r}_1,\omega)G(\mathbf{r}_1,\mathbf{r}',\omega). \tag{2.6}$$

This recursive definition of G can be seen as an infinite series of scattering events caused by the scattering potential $V(\mathbf{r})$, with the propagation of the light in between two scattering events described by the bare Green's function, g. The full Green's function describes all possible paths the light can take through the medium going from $\mathbf{r}'$ to $\mathbf{r}$.

We assume that the scattering in the medium is caused by point scatterers. Therefore the scattering potential $V(\mathbf{r})$ becomes discrete and a function of the positions of all the N independent scatterers, $\mathbf{r}_1 \ldots \mathbf{r}_N$:

$$V(\mathbf{r},\omega) = \sum_{i=1}^{N} V_i(\omega)\delta(\mathbf{r}-\mathbf{r}_i), \tag{2.7}$$

with V_i the strength of the i^{th} scatterer. The distribution of the scatterers in random media is unknown, making it impossible to know the exact form of the scattering potential. For every distribution of scatterers, the scattering potential is different. Therefore we will look at the average field propagator inside random media. We introduce the ensemble average operator which averages over every possible distribution of scatterers,

$$\langle\cdot\rangle \equiv \int d\mathbf{r}_1 \ldots d\mathbf{r}_N P(\mathbf{r}_1 \ldots \mathbf{r}_N)\,[\cdot], \tag{2.8}$$

where $P(\mathbf{r}_1 \ldots \mathbf{r}_N)$ is the probability density of a particular distribution. For a system of statistically independent isotropic point scatterers, we find the average field propagator to be [10]

$$\langle G(\tilde{\mathbf{r}},\omega)\rangle = -\frac{e^{iK(\omega)}}{4\pi\tilde{r}} \equiv -\frac{e^{i\left[k_0 n_{\text{eff}}(\omega)+\frac{i}{2\ell_{\text{ex}}(\omega)}\right]}}{4\pi\tilde{r}}, \tag{2.9}$$

where $k_0 \equiv \omega/c$. The average field propagator in random media is a spherical wave propagating away from the origin, as was also the case with propagation of light through free space. The extinction due scattering of light is included in the effective wave vector $K \equiv k_0 n_{\text{eff}}(\omega) + \frac{i}{2\ell_{\text{ex}}(\omega)}$, with an effective refractive index n_{eff} and an extinction mean free path ℓ_{ex}. In a medium where absorption is absent and where the scatterers are isotropic, ℓ_{ex} is equal to the transport mean free path ℓ_{tr}, which is the average distance light can propagate without being scattered.

2.2.3 The intensity propagator

Although the propagator describes the average propagation of the electric field well, it does not model the diffusion of intensity [7]. The electric field can attain both positive and negative values in contrast to intensities which can only be positive. Averaging over the field does therefore not obey energy conservation. To describe the intensity diffusion, we need to look at the average intensity propagator of light inside random media.

The propagator for the intensity is found by multiplying two full Green's functions before averaging over all realizations of the scattering medium. We define the ensemble averaged intensity propagator $R(\mathbf{r}_a, \mathbf{r}_b, \mathbf{r'}_a, \mathbf{r'}_b, \omega)$,

$$R(\mathbf{r}_a, \mathbf{r'}_a; \mathbf{r}_b, \mathbf{r'}_b, \omega) \equiv \left\langle G(\mathbf{r}_a, \mathbf{r'}_a, \omega) \times G^*(\mathbf{r}_b, \mathbf{r'}_b, \omega) \right\rangle . \tag{2.10}$$

The intensity propagator consists of a sum over all possible paths between two positions, $\mathbf{r}_a$ and $\mathbf{r'}_a$ multiplied by all the paths between $\mathbf{r}_b$ and $\mathbf{r'}_b$. We can discover a huge variety of combinations of paths inside this sum. Some combinations have no common scatterers, making them statistically independent. The sum over all these combinations of paths account for coherent intensity propagation [10]. The intensity of the coherent propagation falls off exponentially with distance, but keeps propagating in the same direction. In this thesis we denote the coherent intensity propagation as ballistic transport. Other combinations of paths do have common scatterers and ask for a careful treatment when we take the ensemble average. A special class of combinations are the paths which propagate along the same scatterers in the exact same order. Multiplication of two of these paths always leads to constructive interference, making them survive the averaging over all different realizations of the medium. These special combinations are called the ladder terms.

Diffusion of light intensity is a result of the ladder terms. To arrive at the intensity diffusion equation, we approximate the propagation of light intensity by only taking the ladder terms into account. This is a good approximation in the weak scattering limit ($k\ell_{\mathrm{tr}} \gg 1$), where the ladder terms are dominant. Furthermore we focus on the slow, long distance behavior of the ladder terms. The intensity propagator in the time domain now reads [10],

$$R(\tilde{\mathbf{r}}, t) = \frac{v_{\mathrm{E}}}{\ell_{\mathrm{tr}}(4Dt)^{3/2}} e^{-\tilde{r}^2/4Dt}, \tag{2.11}$$

where D is the diffusion constant and v_{E} the energy velocity. By taking the derivatives of Eq. 2.11 we find the diffusion equation,

$$\frac{\partial R(\tilde{\mathbf{r}}, t)}{\partial t} = D\nabla^2 R(\tilde{\mathbf{r}}, t) + \text{source}. \tag{2.12}$$

In the rest of the chapter we will consider the stationary case with a monochromatic wave. In this approach the time derivative of the intensity propagator R will become zero.

2.3 Diffusion in a slab

For the diffusion equation found in the previous section, we assumed an infinite medium. In real life the medium will always have finite dimensions. Part of the light is reflected

at the surface, due to the refractive index contrast between the scattering medium and the outside world. Therefore surface effects have to be taken into account to describe the distribution of light intensity inside finite media.

We consider a slab geometry where the lateral dimensions x and y extend to infinity and where the transverse dimension is bounded at $z = 0$ and $z = L$ (see Fig. 2.1). We assume that, with the proper boundary conditions at the surface, Eq. 2.12 is still valid everywhere inside the medium.

2.3.1 Boundary conditions

The boundary conditions at the material surfaces are found by looking at the intensity flux. The flux, $J(\mathbf{s}, \mathbf{r})$, is the rate of energy propagating in a certain direction, $\mathbf{s}$. We can find the current by integrating the flux over all directions taking their directions into account,

$$\mathbf{J}(\mathbf{r}) = \int_0^{2\pi} \int_0^{\pi} d\theta d\phi \sin(\theta) J(\mathbf{s}, \mathbf{r}) \mathbf{s}, \tag{2.13}$$

with $s = (\cos\phi \sin\theta, \sin\phi \sin\theta, \cos\theta)$. If we divide the flux by the average energy velocity v_e we get the specific intensity in the direction of the flux. The total intensity $I(\mathbf{r})$ is found by integrating the specific intensity over all directions,

$$I(\mathbf{r}) = \frac{1}{v_\mathrm{e}} \int_0^{2\pi} \int_0^{\pi} d\theta d\phi \sin(\theta) J(\mathbf{s}, \mathbf{r}). \tag{2.14}$$

Energy conservation relates the current to the intensity; the nett flux across a infinitely small closed surface has to equal the time derivative of the intensity,

$$\nabla \mathbf{J} = -\frac{\partial I}{\partial t}. \tag{2.15}$$

Furthermore we can relate the current with the intensity by using the diffusion equation Eq. 2.12 derived in the previous section. If we combine the diffusion equation with Eq. 2.15 we find,

$$\mathbf{J} = -D \nabla I, \tag{2.16}$$

which is called Fick's law. We assume that the flux leaving the medium is distributed uniformly over all outgoing angles. Part of the outgoing flux is reflected at the surface of the medium, creating an incoming flux which we also assume to be uniformly distributed over all incident angles. The outgoing and incoming flux read,

$$\mathbf{J}_\mathrm{out}(\mathbf{s}, \mathbf{r}) = J_\mathrm{out}/(2\pi), \tag{2.17}$$

and

$$\mathbf{J}_\mathrm{in}(\mathbf{s}, \mathbf{r}) = R J_\mathrm{out}/(2\pi), \tag{2.18}$$

respectively. The reflection coefficient R can be found by integrating the Fresnel reflection coefficients over all angles. Now that the flux is defined we calculate the total intensity

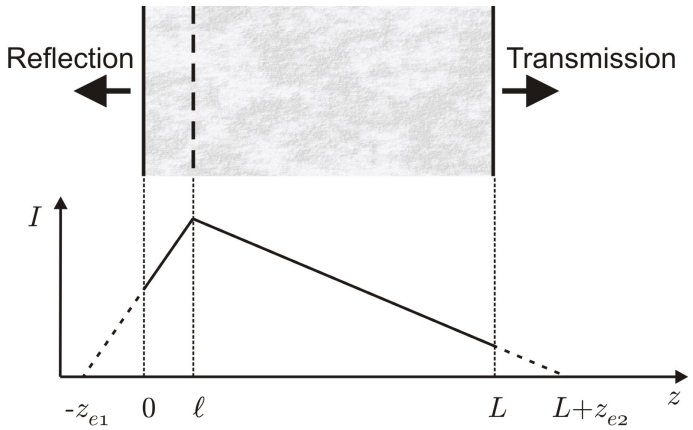

Figure 2.1: Model of diffusion through a slab. In the upper part of the figure, the geometry of the sample is given. The source is approximated by a plane source at $z = \ell_{tr}$, represented by the thick dashed line. In the lower part the steady state intensity is shown. From the plane source the intensity falls off linearly to both sides. If one extrapolates the intensity outside the medium, it becomes zero at $z = -z_{e1}$ and at $z = L + z_{e2}$.

and the nett flux at the left boundary ($z = 0$),

$$I(\mathbf{r}) = \frac{1}{v_{\mathrm{e}}} J_{\mathrm{out}} (1 + R), \tag{2.19}$$

$$\begin{aligned} \nabla I &= \frac{1}{D} \int_0^{2\pi} d\phi J_{\mathrm{out}} \left[\int_0^{\frac{\pi}{2}} d\theta \sin(\theta) \mathbf{s} + \int_{\frac{\pi}{2}}^{\pi} d\theta \sin(\theta) R \mathbf{s} \right] \\ &= \frac{1}{2D} J_{\mathrm{out}} [1 - R] \, \mathbf{e_z}. \end{aligned} \tag{2.20}$$

The boundary condition for the left boundary can be found by combining these two equations,

$$I(\mathbf{r})\big|_{z=0} - z_{\mathrm{e1}} \frac{dI(\mathbf{r})}{dz}\bigg|_{z=0} = 0, \tag{2.21}$$

with the extrapolation length [12, 13] at the left boundary $z_{\mathrm{e1}} \equiv \ell_{\mathrm{tr}} \frac{2}{3} \frac{1+R}{1-R}$. In a similar way we can find the boundary condition for the right boundary at $z = L$,

$$I(\mathbf{r})\big|_{z=L} + z_{\mathrm{e2}} \frac{dI(\mathbf{r})}{dz}\bigg|_{z=L} = 0, \tag{2.22}$$

with $z_{\mathrm{e2}} \equiv \ell_{\mathrm{tr}} \frac{2}{3} \frac{1+R}{1-R}$ the extrapolation length at the right boundary. The reflection coefficient R depends on the conditions at the interface and can be different for the front and back of the sample.

2.3.2 Solving the diffusion equation

Now that we derived the proper boundary conditions, we can solve the stationary diffusion equation for a slab geometry. We only need to define our source of diffusive light. Light entering the sample will not be immediately diffuse. On average, light becomes diffusive

after propagating one transport mean free path ℓ_{tr} through the medium. Therefore we model the diffusive source as a plane source at position $z = \ell_{\text{tr}}$, one mean free path deep inside the sample.

We solve the diffusion equation for two separate ranges, $0 \leq z < \ell_{\text{tr}}$ and $\ell_{\text{tr}} < z \leq L$, using the appropriate boundary conditions found in the previous subsection. Equating the two solutions two each other at $z = \ell_{\text{tr}}$ gives the solution for the intensity,

$$I(z) = \frac{S_0}{D} \begin{cases} \dfrac{L - \ell_{\text{tr}} + z_{\text{e2}}}{L + z_{\text{e1}} + z_{\text{e2}}}(z + z_{\text{e1}}), & 0 \leq z \leq \ell_{\text{tr}} \\ \dfrac{\ell_{\text{tr}} + z_{\text{e1}}}{L + z_{\text{e1}} + z_{\text{e2}}}(L + z_{\text{e2}} - z), & \ell_{\text{tr}} \leq z \leq L. \end{cases} \tag{2.23}$$

From Eq. 2.16 we see that the strength of the source S_0 is given by the total incoming flux J_{in}. The intensity is plotted Fig. 2.1. From the source at $z = l$ the intensity falls off linearly to both sides. If one extrapolates the intensity outside the medium, it becomes zero at $z = -z_{\text{e1}}$ and at $z = L + z_{\text{e2}}$.

2.3.3 Total transmission

A fairly simple experiment that can be performed on a slab of diffusive material is a total transmission experiment. The sample is illuminated from one side and the light is detected on the other side of the sample. To measure the total transmission, the light has to be integrated over all outgoing angles. We define the total transmission T as the total flux at $z = L$ divided by the incident flux S_0. From the intensity distribution inside a slab we can calculate the outgoing flux at the right side of the sample. The total transmission T is found to be

$$T \equiv \frac{\mathbf{J}_{\text{out}}\big|_{z=L}}{S_0} = -\frac{D}{S_0}\frac{\partial I}{\partial z}\bigg|_{z=L} = \frac{\ell_{\text{tr}} + z_{\text{e1}}}{L + z_{\text{e1}} + z_{\text{e2}}}. \tag{2.24}$$

By measuring the total transmission for similar samples with different thicknesses L, it is possible to deduce the transport mean free path ℓ_{tr}.

2.4 Channel mixing

In the previous section we described the ensemble average intensity propagator, leading to the diffusion of intensity. If we consider a single realization of the medium though, we find that the angular intensity is fluctuating as a function of the outgoing angle and the frequency of the light. These spatial fluctuations are caused by interference of the scattered light; light traveling along different paths end up with random phases, amplifying or weakening the local intensity. This granular intensity pattern is known as a speckle pattern. In this section we first discretisize to field contributions on a certain position inside the sample. Then we find the intensity distribution of the speckle pattern.

2.4.1 Scattering channels

In a random scattering medium, light travels along different paths throughout the sample and interferes destructively and constructively at random positions, forming a spatial

speckle pattern. The resultant field, $E(\mathbf{r}_b)$, at a certain position $\mathbf{r}_b$, inside our outside the medium, is a random sum of field contributions, coming from different positions, $\mathbf{r}_a$. In general we write the field $E(\mathbf{r}_b)$ as

$$E(\mathbf{r}_b) = \int G(\mathbf{r}_b, \mathbf{r}_a) S(\mathbf{r}_a) d^3\mathbf{r}_a, \tag{2.25}$$

with $G(\mathbf{r}_b, \mathbf{r}_a)$ the non-averaged Green's function describing the propagation of light from the sources $S(\mathbf{r}_a)$ to the point $\mathbf{r}_b$. This equation is valid for every linear medium.

In the spatial speckle pattern, small correlation areas can be found in the order of $\lambda^2/4$ [7], the average speckle size. We use this spatial intensity correlation to discretize Eq. 2.25, defining a discrete number of incident scattering channels N in analogy to the number of channels supported by a waveguide [14]. We write the resultant field at position $\mathbf{r}_b$ as a discrete random sum by integrating over the correlation areas S_a of the incoming scattering channels

$$\begin{aligned} E(\mathbf{r}_b) \equiv E_b &= \sum_{a=1}^{N} \int_{S_a} G(\mathbf{r}_b, \mathbf{r}_a) d^2\mathbf{r}_a \, |E_a| \, e^{i\phi_a} \\ &\equiv \sum_{a=1}^{N} G_{ba} \, |E_a| \, e^{i\phi_a}. \end{aligned} \tag{2.26}$$

In this equation $|E_a|$ is the amplitude and ϕ_a is the phase of the incoming scattering channel. The complex field transmission coefficient G_{ba} describes the transmission from channel a to position $\mathbf{r}_b$. For an incoming plane wave with a uniform amplitude distribution A, we find E_b to be

$$E_b = A \sum_{a=1}^{N} G_{ba}. \tag{2.27}$$

The field on position $\mathbf{r}_b$ is a sum over N complex field transmission coefficients G_{ba}. In a random system the coefficients G_{ba} are independently drawn from a single circular Gaussian distribution [15].

It should be noted that the scattering channels can also be defined in angular space, where plane waves incident with a certain wave vector k_a represent the scattering channel a. For a large number of channels, the angular definition is equivalent to the position dependent definition of scattering channels.

2.4.2 Speckle intensity distribution

Multiple scattering completely mixes light entering the material through different scattering channels, a process we define as channel mixing. This process results in a speckle pattern. The statistics of the intensity distribution of the speckle pattern, $P_I(I)$, outside a scattering material is well known [15]. We use the same approach to model the intensity distribution inside a scattering medium [15].

In a disorder system it is often allowed to assume that the transmission coefficients are independently drawn from a single circular Gaussian distribution [15]. This assumption can encompasses three different statements:

1. The phase and the amplitude of two different transmission coefficients are statistically independent of each other.
2. The phase and the amplitude of the same transmission coefficient are unrelated to each other.
3. The phases of the different transmission coefficients are distributed uniformly over the interval of -π to π.

From these assumptions we find that $\langle G_{ba} \rangle = 0$ and $\left\langle G_{ba} G^*_{ba'} \right\rangle = \delta_{aa'}$. The probability density function of the field modulus $|E_b|$, which is a sum over N independent transmission coefficients, then reads [15]

$$P_{E_b}(|E_b|) = \frac{2\,|E_b|}{\sigma^2} e^{-|E_b|^2/\sigma^2}. \tag{2.28}$$

The average intensity is found by integrating the probability density function in Eq. 2.28 multiplied by $I_b \equiv |E_b|^2$,

$$\langle I_b \rangle = \int_0^\infty dE_b\, |E_b|^2\, P_{E_b} = \sigma^2 \tag{2.29}$$

To find the intensity distribution we use Eq. 2.28 and substitute $|E_b|^2$ by I_b. Furthermore we introduce the Jacobian equal to $1/(2\,|E_b|)$ which accounts for the coordinate transform from field to intensity. The intensity distribution reads

$$P_{I_0}(I_b) = \frac{1}{I_0} e^{-I_b/I_0}, \tag{2.30}$$

with $I_0 \equiv \langle I_b \rangle$. The intensity distribution is the well known Rayleigh distribution. The fluctuations in this negative exponential distribution are characterized by a variance equal to the mean intensity squared.

2.5 Channel demixing

In the previous section we described the random scattering of light inside a scattering sample with a process called channel mixing; light that enters the sample through different scattering channels is mixed and ends up with random phases and amplitudes. The mixing process inside a scattering disordered material complex and stochastic. Due to the time reversibility of Maxwell's equations, it is always possible to reverse the mixing process, leading to an enhanced intensity at the position where the channels demix.

2.5.1 Principle of channel demixing

The field at a certain position $\mathbf{r}_b$ is a sum over the fields of the incoming scattering channels times their transmission coefficients. For a homogeneous illumination of the sample the field E_b reads:

$$E_b = A \sum_a^N |G_{ba}|\, e^{i(\phi_{ba} - \phi_a)}, \tag{2.31}$$

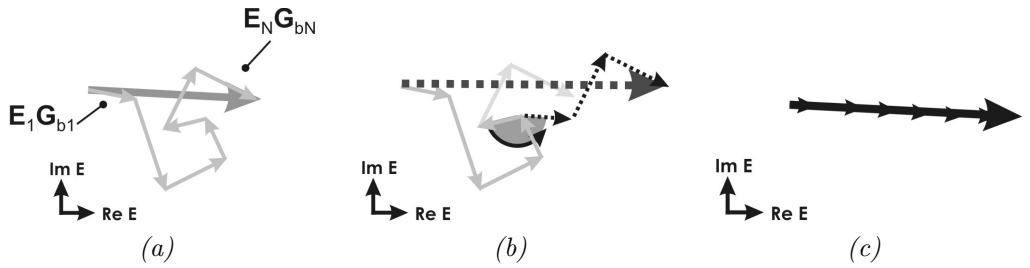

*Figure 2.2: Principle of channel demixing. In this figure we see a complex amplitude representation of the field at the target position. In (**a**) the initial situation is depicted. All incoming channels randomly contribute to the total field. To find the field transmission coefficient we cycle the phase of a single incident channel as is seen in (**b**). The dashed lines present the field after one of the channels is set to its optimal position. Once all transmission coefficients are known, we demix the channels by setting the right phase shifts for each incident channel. All the incident channels now arrive at the target position with the same phase and interfere constructively, leading to a enhanced intensity (**c**).*

with ϕ_{ba} the phase of the transmission coefficient, and ϕ_a the phase of the light entering the sample through channel a. The interference pattern is changed completely when we modify the phase of one or more channels. The amplitude of the field E_b is maximized if ϕ_a is exactly the oppisite of ϕ_{ba} for all channels a; that is, if all channels interfere constructively at the position $\mathbf{r}_b$. By changing the phase of each incident channel such that it compensates for the phase lag ϕ_{ba} introduced by scattering , we can optimize the field amplitude E_b. We effectively reverse the mixing process of the channels at a desired position $\mathbf{r}$, or in other words, demix the channels.

In an experiment, the transmission coefficients are not known in advance. To find the optimized linear combination of incident channels, the phases of the transmission coefficients have to be measured. The phases are found by looking at the interference of a single channel with the background intensity. When we change the phase of channel a, the intensity at position $\mathbf{r}_b$ responds as

$$I_b = I_{bg} + 2A\,|G_{ba}|\,|E^*_{b\bar{a}}|\cos(\phi_a - \phi_{b\bar{a}}), \tag{2.32}$$

with

$$E_{b\bar{a}} \equiv A\sum_{a'\neq a}^{N} G_{ba'}e^{i\phi_{a'}}. \tag{2.33}$$

The intensity $I_{bg} \equiv |E_{b\bar{a}}|^2 + A^2\,|G_{ba}|^2$ is the already present background with which the channel a interferes. Modulating the phase of channel a results in a sinusoidal intensity response from which we deduce ϕ_a.

In Fig. 2.2 the principle of channel demixing is sketched. Initially, each incoming channel randomly contributes to the field at the target position, as is seen in (**a**). We change the phase of one incident channel at the time. The modulated channel interferes with the already present background of all the other incident channels (see (**b**)). This interference results in a sinusoidal intensity response from which we can deduce the complex field transmission coefficient G_{ba} for the modulated channel. Once all transmission

coefficients are known, we demix the channels by setting the $\phi_a = -\phi_{ba}$. All the incident channels now arrive at the target position with the same phase and interfere constructively (**c**), leading to the maximal intensity.

Channel demixing of light at a position behind a strongly scattering sample was first demonstrated by Vellekoop and Mosk [6]. In their experiments, they reversed the mixing process by shaping the incident wavefront. Scattering inside the sample formed the shaped wavefront into a diffraction limited spot, at a position behind the sample.

2.5.2 Maximum intensity enhancement

The maximal intensity that can be reached by channel demixing is related to the number of controlled incident channels, N. In this section we will derive an equation for the maximum enhancement, defined as the ratio between the optimal intensity and the speckle averaged intensity. We assume a homogeneous illumination of the different incident channels with an amplitude of A. The intensity at the target position, I_b, is written as

$$I_b \equiv |\mathbf{E}_b|^2 = A^2 \sum_{a=1}^{N} G_{ba} e^{i\phi_a} \sum_{a'=1}^{N} G^*_{ba'} e^{-i\phi_{a'}}. \tag{2.34}$$

We examine the ensemble averaged intensity at the target position. The transmission coefficients G_{ba} are statistically independent and are taken from a circular Gaussian distribution [15]. Therefore the ensemble averaged value of G_{ba} is zero, $\langle G_{ba} \rangle = 0$, and the cross terms ($G_{ba} G^*_{ba'}$ with $a \neq a'$) do not contribute to the ensemble averaged intensity. Averaging and rewriting Eq. 2.34 into a sum with $a = a'$ and a sum with $a \neq a'$ gives

$$\langle I_b \rangle = A^2 \left[\sum_{a}^{N} \left\langle |G_{ba}|^2 \right\rangle + \sum_{a}^{N} \sum_{a \neq a'}^{N} \left\langle G_{ba} e^{i\phi_a} \right\rangle \left\langle G^*_{ba} e^{-i\phi'_a} \right\rangle \right]. \tag{2.35}$$

We first consider the case where we illuminate the scattering material with a random linear combination of incident channels; the phases ϕ_a and $\phi_{a'}$ of the different incident channels are independent and are not related to the transmission coefficients G_{ba}. The ensemble averaged sum over the cross terms with $a \neq a'$ becomes zero, giving us the ensemble averaged intensity for random illumination, $\langle I_{b,0} \rangle$

$$\langle I_{b,0} \rangle = A^2 N \left\langle |G_{ba}|^2 \right\rangle. \tag{2.36}$$

Next we treat the case where we demix the channels at the target position $\mathbf{r}_b$. Instead of a random linear combination of incident channels, we choose the phases for each incident channel such that it compensates for the phase retardation inside the sample; $\phi_a = -\phi_{ba}$. All channels now interfere constructively at the target position giving a maximal intensity, $I_{b,\max}$

$$\langle I_{b,\max} \rangle = A^2 N \left[\left\langle |G_{ba}|^2 \right\rangle + (N-1) \left\langle |G_{ba}| \right\rangle^2 \right]. \tag{2.37}$$

The theoretical maximum enhancement η is defined as the ratio between the maximal intensity when all channels interfere constructively at the target position and the ensemble

averaged intensity. From the complex Gaussian probability distribution for G_{ba} we find the ratio between $\langle|G_{ba}|\rangle^2$ and $\left\langle|G_{ba}|^2\right\rangle$ to be $\pi/4$. The enhancement now reads

$$\eta \equiv \frac{\langle I_{b,\max}\rangle}{\langle I_{b,0}\rangle} = \frac{\pi}{4}(N-1)+1. \tag{2.38}$$

From this equation it is seen that the maximal intensity enhancement is a linear function that only depends on the number of controlled channels. Controlling 1250 independent channels, for example, leads to an intensity enhancement of almost a factor of 1000 [6].

2.5.3 Multimode optimization

The maximal enhancement derived in the previous section can only be reached when a single optical mode contributes to the recorded intensity. A detection of multiple polarizations, for example, leads to contributions of multiple modes. If the intensity of multiple modes is recorded simultaneously during the measurement of the transmission coefficients G_{ba}, the incident channels will not demix into one mode but distribute over multiple modes. For M contributing modes, the initial total intensity is equal to

$$\langle I_{b,0}\rangle = \sum_{b}^{M}\left(A^2N^2\left\langle|G_{ba}|^2\right\rangle\right). \tag{2.39}$$

It is now not longer possible to determine G_{ba} from the measured interference between the modulated channel a and the background field $E_{b\bar{a}}$. Our channel demixing method finds a solution which overlaps with all M measured modes. We write G_{ba} as

$$d_a G_{ba} + (1-d_a)G_{ba} \tag{2.40}$$

where d_a is the normalized inner product of the G_{ba} with the present background $E_{b\bar{a}}$. When the statistical properties of all modes are equal, we find that $d_a = 1/\sqrt{M}$. The second term in Eq. 2.40 stands orthogonal to $E_{b\bar{a}}$ and does not contribute to the measurements. The average intensity after constructing the optimal combination of incident channels is therefore

$$\langle I_{b,\max}\rangle = A^2N^2\left[\left\langle|G_{ba}|^2\right\rangle + d_a^2(N-1)\left\langle|G_{ba}|\right\rangle^2\right]. \tag{2.41}$$

We now find the maximal possible intensity enhancement, for a multimode optimization of M modes:

$$\eta = \frac{\pi}{4}\frac{(N-1)}{M}+1. \tag{2.42}$$

For $N >> 1$, the maximal enhancement is proportional to the number of controlled incident channels N and is inversely proportional to the number of detected modes M.

In Chapter 5 we discuss channel demixing experiments on scattering samples doped with fluorescent probes. These probes are used to detect the intensity at a position inside the opaque samples. Due to the size of the probes, we detect 6 individual modes at the same time. In the experiments we control 640 incident channels. We therefore expect a theoretical intensity enhancement of 85 in these experiments.

2.6 Conclusions

It was shown that multiple scattering of light leads to diffusion of intensity. The well known diffusion equation was found by looking at the ladder terms of the average intensity propagator. We applied the diffusion equation to a slab geometry and the proper boundary conditions were found.

Multiple scattering mixes light that enters the material through different scattering channels. This channel mixing results in a granular intensity pattern inside and outside the scattering medium. We derived the probability density function for the intensity distribution. It was shown that the intensity follows a Rayleigh distribution.

It is possible to invert the channel mixing process. We explained a method to demix the channels at any desired position inside or outside the medium by adjusting the phase of each incident channel. Demixing the channels leads to a local intensity enhancement because all channels interfere constructively on a certain target position. We calculated the maximal intensity enhancement for one target and for a multimode optimization. The maximal enhancement is proportional to the number of controlled incident channels and is inversely proportional to the number of optimized modes.

CHAPTER 3

Instrumentation

3.1 Introduction

In this chapter we focus on the experimental apparatus used for the channel demixing experiments which are described in chapter 5. We have build an apparatus that generates shaped incoming wavefronts, projects them onto our samples and detects the returning fluorescent light. The intensity of the fluorescent light is used as a feedback to shape the incoming wavefronts.

The modulation of the incoming light is an important part of our setup and will be discussed in section 3.2. In that section we present a novel technique which solves existing cross-modulation problems in spatial light modulators. In section 3.3 the technical details of the experimental apparatus are described. This chapter ends with section 3.4 where the procedure of the wavefront construction is discussed.

3.2 Full spatial phase and amplitude control[1]

We present a method for full spatial phase and amplitude control of a laser beam using a twisted nematic liquid crystal display together with a spatial filter. By spatial filtering we combine four neighboring pixels into one superpixel. With each superpixel we are able to independently modulate the phase and the amplitude of light. Our technique does not impose special requirements on the spatial light modulator and should work for any type of spatial light modulator.

[1]Section 3.2 will be submitted for publication as "*Spatial amplitude and phase modulation using commercial twisted nematic lcds*" by E.G. van Putten, I.M. Vellekoop and A.P. Mosk [16].

3.2.1 Introduction

Several exciting new applications of optics rely on spatial phase and amplitude control of light. In adaptive optics, light is modulated to correct for abberations in a variety of optical systems such as the human eye [17] or the atmosphere [18]. Holography is another area of optics which relies on the spatial modulation of light. Holographic data storage [19], 3D display technology [20], and diffractive optical elements [21] are just a few examples of the many exciting topics in holography that use complex modulation of light. Very recently, it was shown that opaque strongly scattering materials can focus light by sending in spatially shaped wavefronts [6].

Because of their high optical efficiency, high number of degrees of freedom, and wide availability, liquid crystal spatial light modulators (LC SLMs) are used in many setups where modulation of light is required. A SLM is a device that can modulate the phase and the amplitude of light at refresh rates of ∼50 Hz and at resolutions in the order of 10^6 pixels. The light is modulated according to a fixed spatial pattern given by the pixels of the SLM. Aside from their advantages, commercially available SLMs have some limitations. In most SLMs the modulation of phase is coupled to a modulation of the polarization. This makes it hard to selectively modulate the phase or the amplitude.

Several techniques have been proposed to achieve independent spatial phase and amplitude control using a SLM. Examples are setups where two SLMs are used to balance out the cross modulation [22, 23], double pass configurations where the light propagates twice through the same SLM [24, 25], and double pixel setups which divide the encoding of complex values over two neighboring pixels [26–28]. Each of these techniques has its specific disadvantages. The use of two SLMs in one setup [22, 23] requires more space and a sensitive alignment . Double pass configurations [24, 25] double the phase modulation capacities, usually delivering a full 2π phase shift. Unfortunately though, to keep the amplitude constant, the SLM has to work in a mostly-phase condition which requires light of a specific elliptical polarization. Double pixel setups [26–28] also require special modulation properties of the SLM that can be achieved by sending in light under a certain specific polarizations. Small deviations from these polarizations already modify the modulation properties, leading to drift in the achieved amplitudes and phases.

We propose a novel modulation technique to achieve complex modulation of light using a SLM together with a spatial filter. This technique does not pose special requirements on the SLM or the incoming light, making our technique more widely applicable than previous techniques. In our experiments we used a HoloEye LC-R 2500 twisted nematic liquid crystal display (TN-LCD) which has 1024x768 pixels and which can modulate with 8-bit accuracy (256 voltage levels). This SLM has a strong cross-modulation between the phase and the polarization of the light. We demonstrate the use of this SLM to independently modulate phase and amplitude.

3.2.2 Cross-modulation in TN-LCDs

Twisted nematic liquid crystal displays (TN-LCDs) owe their name to the helical structure formed by the molecules inside the LCD cells, in absence of an electrical field. When a voltage is applied over the edges of the LCD cell, the molecules orient themselves in the direction of the electric field and the twisted structure will disappear. By changing the

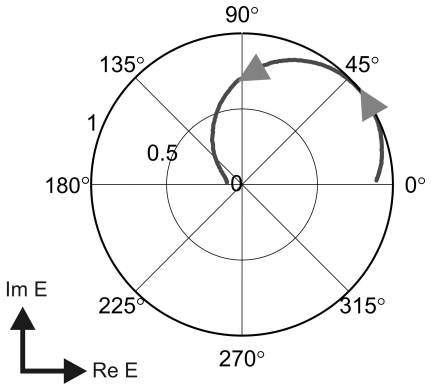

Figure 3.1: Experimental modulation plot for the SLM, illuminated with vertical polarized light. After modulation, the light with a horizontal polarization is detected. This plot shows the amplitude versus the phase modulation. The modulation voltage increases in the direction of the gray arrows.

voltage over the cells, the internal structure can be changed continuously from a twisted to a straight alignment of the molecules.

A TN-LCD rotates the polarization of light in a controllable way. The twisted structure inside a TN-LCD cell acts as a waveguide to the light and the more profound the twisted structure is present, the more the polarization rotates. A TN-LCD in combination with a set of polarizers is widely used to modulate the intensity of light (for example in LCD-TV screens and video projectors). In spatial light modulators (SLMs) TN-LCDs are often used to modulate the phase of light. The optical path length inside the cell will vary with polarization of the light, causing a adjustable phase shift. When independent control of phase and polarization is required, the cross modulation is a downside of TN-LCDs.

To determine the modulation curve of our SLM, we used a diffractive technique where we place a binary grating with a 50% duty cycle [29] on the display. Using a polarizing beam splitter we illuminate the SLM with vertically polarized light and detect the horizontally polarized component of the modulated light. We measure the intensity in the 0^{th} order of the far-field diffraction pattern for different contrast levels of the grating. The contrast difference is achieved by keeping the notches of the grating steady at a constant value while we cycle the voltage values of the rules of the grating over the complete voltage range in 255 steps. We determine the real and imaginary parts of the field as a function of the voltage level encoded on the pixels, by comparing the measured 0^{th} order intensity for different pixel values on both the notches and the rules of the grating. The results of these measurements are plotted in Fig. 3.1. Applying a voltage of 0 we start with a 0 phase shift. With increasing voltage, the phase is modulated from 0 up to π while the amplitude first becomes larger and then decreases. The deviation of the modulation curve from a concentric circle around 0 is a clear indication of cross-modulation.

3.2.3 Decoupling of phase and amplitude by coupling of multiple pixels

By combining four neighboring pixels into one superpixel, we decouple the modulation of the phase and the amplitude and achieve full independent phase and amplitude control of light. Any arbitrary complex amplitude can be synthesized while each individual pixel on

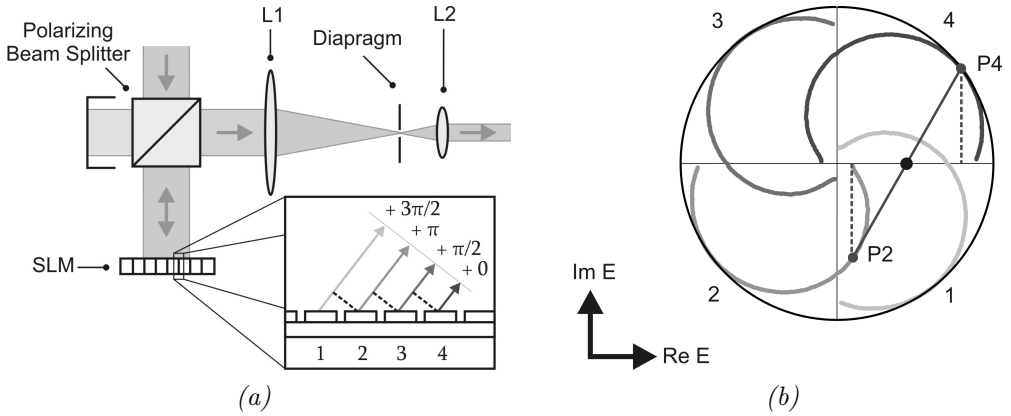

Figure 3.2: Modulation technique to decouple phase and amplitude modulation. In (a) we show the experimental setup. Four neighboring pixels, pixels 1, 2, 3, and 4, are combined to one superpixel which can modulate one complex value. The modulated light is focussed by a lens, L1. A diaphragm is used to spatially filter the light. The diaphragm is positioned so that light under a certain angle is transmitted. This angle is chosen such that in the horizontal dimension, two neighboring pixels on the SLM are exactly $\pi/2$ out of phase with each other. A lens, L2, is used to collimate the beam again. The phase differences between neighboring pixels is $\pi/2$ as is seen in the inset of (a). The molation responses of the pixels are shifted because of the phase differences. In (b) we show the response curves of the pixels 1, 2, 3, and 4, which are shifted $\pi/2$ with respect to each other. The numbers outside the polar plot connect the pixel numbers to their modulation responses.

the SLM is still constrained to its limited complex response, as shown in Fig. 3.1.

The principle of the modulation technique is sketched in Fig. 3.2. A monochromatic beam of light is incident normal to the SLM surface. The modulated light is reflected from the SLM. We choose an observation plane at which the contribution of each neighboring pixel is $\pi/2$ out of phase, as can be seen in the inset of Fig. 3.2 **(a)**. The fields from the individual pixels are superposed using a spatial filter. By choosing the correct combination of pixel values, any complex value of the total field can be synthesized. The electric field coming from one superpixel, E_{sp}, can be written as the sum of the fields, E_1, E_2, E_3, and E_4, coming from the four different pixels. Behind the spatial filter, E_{sp} is given by:

$$\begin{aligned} E_{\mathrm{sp}} &= \left(E_1 e^{i\frac{3}{2}\pi} + E_2 e^{i\pi} + E_3 e^{i\frac{1}{2}\pi} + E_4\right) \\ &= (E_{4r} - E_{2r}) + i\,(E_{3r} - E_{1r}) \\ &\quad + (E_{1i} - E_{3i}) + i\,(E_{4i} - E_{2i})\,, \end{aligned} \tag{3.1}$$

where the indices r and i refer to the real and the imaginary part of the field. We combine pixels 2 and 4 to achieve a perfect amplitude-only modulation on the real axis. The voltages on pixels 2 and 4 are chosen such that the imaginary parts of the modulated fields exactly cancel each other while the real parts add up to the desired real part of E_{mp}. From the geometrical construction shown in Fig. 3.2 **(b)** it can be seen how we modulate a point on the real axis, $(\mathrm{Re}(\mathrm{P}_2)+\mathrm{Re}(\mathrm{P}_4))/2$, by choosing $\mathrm{Im}(\mathrm{P}_2)$ opposite to $\mathrm{Im}(\mathrm{P}_4)$. To modulate the imaginary part of E_{mp}, pixels 1 and 3 are encoded according to the same method. It is always possible to find pixels values with exactly opposite imaginary parts.

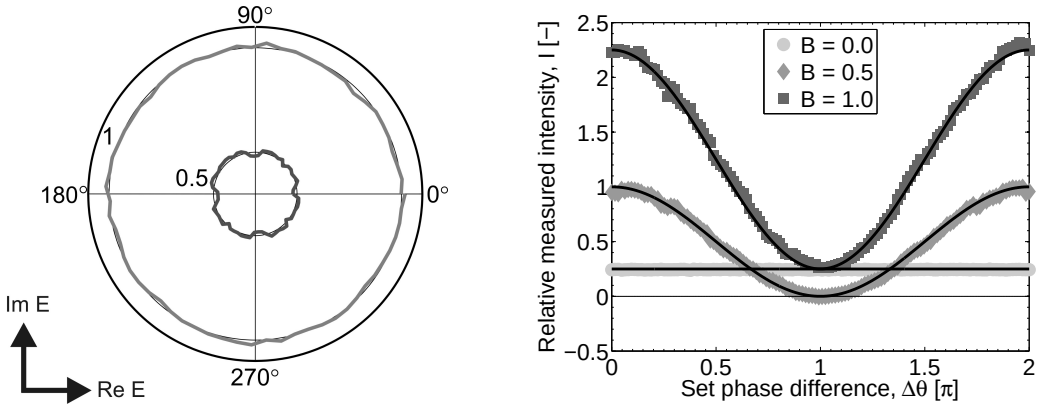

Figure 3.3: Results of the measurements to demonstrate the independent phase and amplitude modulation. In (a) we see the relative amplitude from the intensity measurements as a function of the programmed phase of the plane wave. We did the measurements for different amplitudes. The dark gray line represents the measurements for a relative amplitude of 0.5 and the light gray line for a relative amplitude of 1.0. In (b) we show the relative measured intensity of a grating interference experiment. The intensities are plotted as a function of the set phase difference $\Delta\theta$. The experiment was done for multiple amplitude differences between the rules and the notches of the grating. The solid lines represent the expected intensities.

The only requirement posed on the SLM is that at least one of the field components have to vary when the pixel voltages are changed.

As a technical note, we reconfigured the gamma lookup curve of the modulation electronics after the calibration measurements. Using our modulation technique, a linear increase in pixel values now results in a linear amplitude modulation on the real axis (using pixels 2 and 4) or on the imaginary axis (using pixels 1 and 3). Any complex value, $\mathbf{C}$, can be modulated onto a macro pixel by simply putting the values Im($\mathbf{C}$), Re($\mathbf{C}$), -Im($\mathbf{C}$), and -Re($\mathbf{C}$) on the four distinct pixels. No calculations have to be performed on the PC because all calibrations are stored in the modulation electronics.

3.2.4 Demonstration of modulation technique

We tested the modulation technique with the setup depicted in Fig. 3.2 **(a)**. We placed an extra lens and a CCD camera behind the spatial filter to detect the light in the far-field.

First we demonstrate the decoupling of the phase and amplitude modulation. We encoded the same amplitudes and phases on all superpixels of the SLM, forming a plane light wave. The plane wave was then focussed onto the CCD camera. We measured the intensity while changing the phase and amplitude of the plane wave. In Fig. 3.3 **(a)** the relative amplitudes from the intensity measurements are plotted against the phase of the plane wave. For different amplitude modulations, the phase is cycled from 0 to 2π. It is seen from the results, that we modulate the phase while keeping the amplitude of the light constant within 2.5 %.

Next we show that the set phase modulation is in agreement with the measured phase

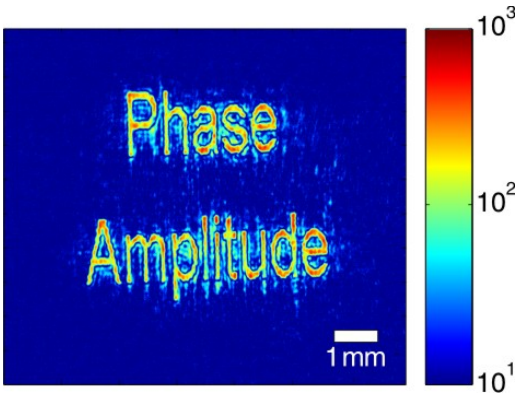

Figure 3.4: Demonstration of complex modulation using the novel modulation technique. In this experiment we encoded a fourier transform of an image onto the SLM and reconstructed the image in the far field. This plot shows the measured intensity in the far field on a logarithmic scale. The intensities are in counts/milliseconds.

modulation. We placed a binary grating with a 50% duty cycle on the SLM. We modified the contrast by keeping one part of the grating constant at a relative amplitude, A, of 0.5 while changing the relative amplitude of the other part, B between 0 and 1. We change the phase difference between the two parts of the grating, $\Delta\theta$, from 0 to 2π. Because of interference, the recorded intensity, I, at the CCD camera will change as a function of A,B, and $\Delta\theta$ in the following way:

$$I = A^2 + B^2 + 2ABcos(\Delta\theta). \tag{3.2}$$

In Fig. 3.3 **(b)** the results are presented for three different values of B. The measured intensities fluctuate as a function set phase difference. The interference follows the theory well, demonstrating an independent phase modulation for different amplitudes. Although originally we could not achieve a full 2π phase shift, we were able to modulate the light from 0 to 2π using the new modulation technique.

Finally we demonstrate complex spatial modulation of light. We encoded the fourier transform of an image onto the SLM. The original image is reconstructed in the far-field and was recorded by the CCD camera. In Fig. 3.4 the reconstructed intensity is shown on a logarithmic scale. The letters in the image stand out with high contrast. Around the letters, small areas containing noise are seen. The relative intensity of the noise is smaller than 10%.

3.2.5 Conclusions

We have presented a novel approach to achieve full independent spatial phase and amplitude control using a twisted nematic liquid crystal display together with a spatial filter. Our novel modulation scheme combines four neighboring pixels into one superpixel. Each superpixel is able to independently generate any complex amplitude value. We demonstrated that we were able to freely modulate the phase over a range of 2π while keeping the amplitude of the light constant within 2.5%. Furthermore we showed that we could achieve a spatially complex modulation of the light with a high resolution.

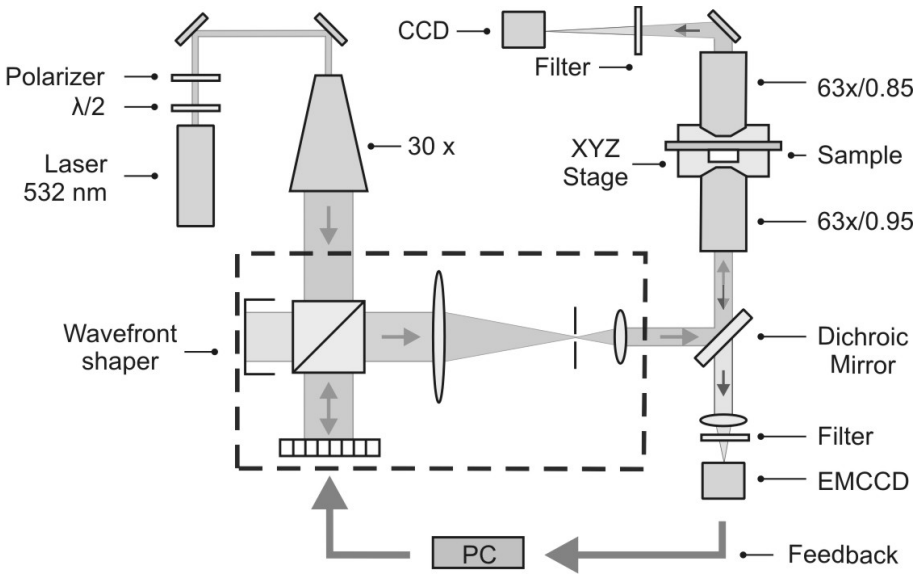

Figure 3.5: Sketch of the experimental setup. A beam coming from a CW-laser ($\lambda = 532\,\mathrm{nm}$) is expanded by a beam expander. The expanded beam is modulated by a wavefront shaper. The SLM inside the wavefront shaper is imaged onto the entrance pupil of the microscope objective using a 2:1 demagnifying telescope. The microscope objective focusses the light onto the sample, thereby mapping the segments of the SLM to modes in k-space. The same microscope objective collects the reflected excitation light and the fluorescent light. The fluorescent light is separated by a dichroic mirror and a bandpass filter. A lens is used to focus the fluorescent light onto a EMCCD camera where it is used as a feedback to control the SLM. A second microscope objective is placed behind the sample to image the substrate side using a CCD.

The presented modulation technique can be used with any SLM. No special modulation response is needed, therefore the illumination light can have linear polarization. This polarization makes a relative simple calibration possible. Using linearly polarized light, the setup can easily be expanded to control two independent polarizations with two SLMs.

3.3 Light delivery and detection

The modulation setup, discussed in the previous section, forms the most important part of our experimental apparatus. We incorporate this wavefront shaper into a larger setup where we magnify the laser beam to the right size, control the illumination of the sample, and detect the returning fluorescent light. In this section we will discuss the technical details of this experimental apparatus.

The setup used in the channel demixing experiments is shown in Fig. 3.5. We use a continuous wave laser with a wavelength of 532 nm (Compass 315M-100 from Coherent). The light propagates through a half-wave plate and a polarizer to get a linear polarized beam with a controllable intensity. Using a beam expander, the beam is magnified 30 times and is send into a wavefront shaper. This wavefront shaper is the same apparatus which is described in section 3.2. The wavefront shaper has a spatial resolution of 1024 x 768 pixels, but in our experiments we group multiple pixels into larger square segments

to decrease the wavefront construction time.

The SLM inside the wavefront shaper is imaged onto the entrance pupil of the microscope objective using a 2:1 demagnifying telescope. The microscope objective (infinity corrected 63x/NA=0.95 from Zeiss) focusses the light onto the sample, thereby mapping the segments of the SLM to modes in k-space. The position of the sample can be controlled in three dimensions by an XYZ piezo nano-positioning stage (P-611.3S NanoCube from Physik Instrumente).

Reflected light from the sample and fluorescent light coming from the probes inside the sample is collected by the same microscope objective with which we illuminate the sample. The fluorescent light is separated by a dichroic mirror (Semrock FF562-Di02-25x36) and a 593nm bandpass filter (Semrock FF01-593/40-25) which only transmits $1\cdot 10^{-7}\%$ of the excitation light. The fluorescent light is projected onto a electron multiplying charge-coupled device (EMCCD, Luca^{em} DL-658M from Andor Technology plc). The camera image is analyzed by a PC that controls the SLM. A second microscope objective (63x/NA=0.85 from Linos) is placed behind the sample and is used to image the substrate side with a charge-coupled device (CCD, Dolphin F-145B from Allied Vision Technologies). The image of this side of the sample is merely used for testing purposes and is not used as a feedback to control the SLM.

3.4 Wavefront construction and data acquisition

The optimal wavefront which inverts the diffusion of light inside the sample is not known in advance of the experiment and is determined experimentally. The channel demixing method, as explained in section 2.5, is applied using a stepwise sequential algorithm as was demonstrated earlier by Vellekoop and Mosk [6] in their inverse diffusion experiments.

The pixels of the SLM are grouped into larger square segments, thereby decreasing the resolution of the wavefront and speeding up the wavefront construction. A typical construction of a wavefront with 640 independent segments, takes about 15 to 20 minutes. When the phase of one of these segment is changed continuously, the intensity response at the position of the fluorescent probe follows a sinusoidal curve. The computer consecutively cycles the phase of each segment from 0 to 2π while the fluorescent response of the probes inside the sample is monitored by an EMCCD camera. The total intensity in the diffusive spot of fluorescent light is determined by summing the intensity in the camera image. The measurements are fitted with a sinusoidal function to find the optimal phase delay for the segment. At this optimal phase, the contribution of the segment interferes constructively with the already present diffusive background. The phase delay is reset to 0 before advancing to the next segment.

The local intensity inside our samples is detected by probes. The degradation of these probes, scale with the amount of excitation intensity; the more light the probes absorb, the faster they degrade. Therefore we choose to use the stepwise sequential algorithm to construct our wavefronts. If we use the stepwise sequential algorithm, the intensity at the position of the probe does not increase substantially until the optimal phase delay for each segment of the wavefront is determined. There are also other algorithms available [30]. With these algorithms, the intensity at the target position increases continuously during the wavefront construction, degrading the probes faster than the stepwise sequential

algorithm. We found these algorithms to be unsuitable for our experiments.

3.5 Conclusions

In this chapter we discussed the instrumentation for the channel demixing experiments. We demonstrated a novel modulation technique to achieve full spatial independent control of the phase and the amplitude of the light using a liquid crystal SLM and a spatial filter. Furthermore we discussed the experimental apparatus that is used to perform channel demixing inside turbid media. We are able to illuminate the sample with a shaped beam and detect the sparse fluorescence emitted by probes with a sensitive EMCCD camera. A computer analyzes the camera image in real time and feedbacks to the SLM to shape the wavefront. A stepwise sequential algorithm is used to shape the wavefront to invert the diffusion and focus the light at a target position deeply inside the sample.

CHAPTER 4

Sample Fabrication and Characterization

4.1 Introduction

We want to show that it is possible to bring light to a certain target position inside a opaque turbid medium by sending in a specially shaped wavefront. In order to demonstrate this technique to enhance the intensity at a position inside a turbid medium, we need to have strongly scattering samples doped with fluorescent spheres. We have fabricated the samples ourself during the course of this project. The samples are strongly scattering with a transport mean free path in the order of the wavelength. In this chapter the fabrication and characterization of the samples are addressed.

To show an intensity enhancement inside the samples, we need to be able to detect the amount of light at the target position. The samples also need to be opaque and the samples should not absorb the light with which we illuminated them. A flat sample surface is desirable for an accurate determination of the sample thickness, but it is not required for the experiment. To detect the local intensity deeply inside our samples fluorescent microspheres were placed at the target positions. The microspheres act as probes for the excitation light. To make the samples opaque and non absorbing, we choose to make our sample out of a strongly scattering material. In order to hide the probes inside the scattering layer, a minimal layer thickness of several transport mean free paths is required.

Strong scattering of light is usually achieved by inhomogeneous materials with large variations in refractive index. Powders of gallium arsenide [31], titanium dioxide [32], zinc oxide [33], and porous structures of gallium phosphide [11] are all good examples of materials known to strongly scatter light. We initially made samples out of titanium dioxide pigment, but unfortunately the fluorescent emission from the probes was overwhelmed by the luminescence of the pigment. Therefore zinc oxide (ZnO) pigment was chosen as a scattering material for our samples, as it does not show any luminescence at the emission

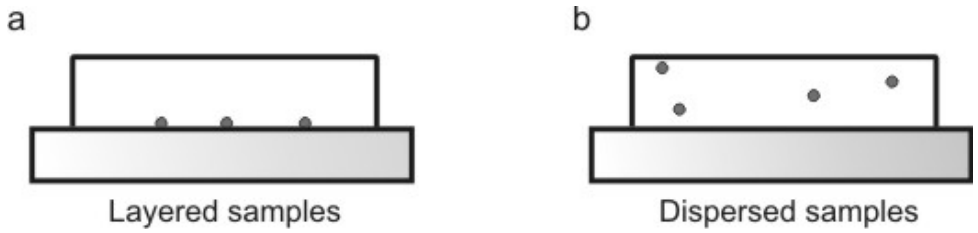

Figure 4.1: Schematic sketch of a layered and a dispersed sample. In (a) a layered sample is depicted. The fluorescent microspheres are placed at the boundary of the ZnO-layer and the glass substrate. A dispersed sample is shown in (b). Here the fluorescent microspheres are dispersed throughout the ZnO-layer.

spectrum of the probes. The lack of background luminescence permits one to resolve the probes inside the sample by looking at the fluorescent emission. To make a smooth scattering layer, one can make a paint by suspending the pigment into an polymer binder like acrylic. Unfortunately we found that most binders show large luminescence, making them unsuitable for our samples. To avoid a large background fluorescence, we choose to make a paint by suspending ZnO pigment into demineralized water. Lacking a binder agent, the scattering layers are fragile and granular instead of smooth and robust.

Two different groups of samples were fabricated. The first group of samples, which we call the layered samples, consist of a glass substrate covered with fluorescent microspheres. A strongly scattering layer of ZnO is deposited on the glass substrate to cover the microspheres (see Fig. 4.1**a**). The second group of samples are called the dispersed samples. These samples also consist of a layer of ZnO on top of a glass substrate, but now the microspheres are dispersed throughout the ZnO-layer (see Fig. 4.1**b**).

In section 4.2 we discuss the procedure used to fabricate the samples. The characterization of the samples is addressed in section 4.3.

4.2 Fabrication procedure

In this section we address the fabrication of both groups. We start with a stepwise explanation of the fabrication procedure of the layered samples. The fabrication of the dispersed samples is very similar to the fabrication procedure of the layered samples and some of the fabrication steps are completely the same. For the fabrication procedure of the dispersed samples we only address the deviating steps.

4.2.1 Layered samples

To fabricate the layered samples we performed the following steps:

1. **Substrate cleaning**
   We began by cleaning the glass substrates thoroughly. Standard 40 x 24 mm^2 microscope coverglasses with a thickness of 160 μm were used as substrates for the samples. First we sprayed acetone onto the substrates to remove any residual organic material and then we rinsed off the acetone with isopropanol and water. The glass substrates were placed aside for half an hour in the open air to dry.

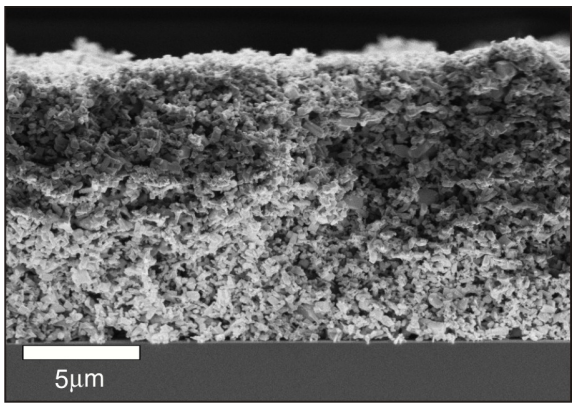

Figure 4.2: Scanning electron micrograph of the cross section of one of our samples. The upper side of the image shows the strongly disordered 13 µm ZnO layer. The bottom side shows a part of the microscope coverglass.

2. **Microsphere preparation**
   The next step is the deposition of the fluorescent microspheres. We started with a commercially available fluorescent polymer suspension from Duke Scientific Corporation [34]. This solution consists of a fluorescent microspheres with a specified diameter of 300 ± 15 nm suspended in deionized water. In each milliliter suspension we have $6.7{\cdot}10^{11}$ microspheres. Before use, the suspension was resuspended by gently rolling and swirling the bottle for half an hour using a rollerbank followed by a brief immersion in a ultrasonic bath. Subsequently we diluted the microsphere suspension a factor 10^5 by adding 2.5 µl of the suspension to 250 ml demineralized water. We placed the cleaned glass substrates in a petri dish and pored the diluted suspension of microspheres in the petri dish. The petri dish was placed in an oven at a temperature of 40 °C. After one day all the water was evaporated and the substrates were covered with the fluorescent microspheres. The average distance between the deposited microspheres was found to be in the order of 10 µm.

3. **ZnO-paint preparation**
   We continued with the preparation of a ZnO-paint. We used commercially available ZnO powder from Aldrich [35] with an average grain size of 200 nm. A suspension was made by mixing ZnO powder with water. We used 8.5 volume percent of ZnO in water. The solution was stirred on a rollerbank and placed in a ultrasonic bath, both for 30 minutes.

4. **Layer fabrication**
   Using an airbrush [36], we sprayed the ZnO-paint onto the glass substrates. The air pressure was set to 2.3 bar. Opaque layers with thicknesses of several micrometers were created. The samples were left to dry horizontally for two hours to let the water evaporate. After drying, a disordered layer of ZnO pigment remained. In Fig. 4.2 we show a scanning electron micrograph of the cross section of one of the samples. The top side of the image shows the strongly disordered 13 µm ZnO layer. The bottom side shows a part of the microscope coverglass.

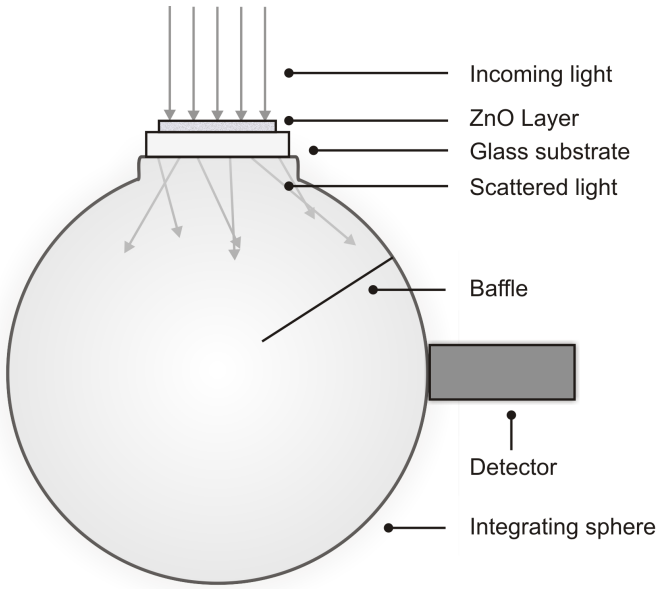

Figure 4.3: Schematic view of the setup used for total transmission measurements. The sample is placed on top of the integrating sphere. Incident light is scattered by the ZnO layer of the sample. The transmitted light is collected in the integrating sphere were it is scattered multiple times before hitting the detector. The partition inside the sphere, called the baffle, prevents light from hitting the detector without scattering.

4.2.2 Dispersed samples

For the fabrication of the dispersed samples, we followed the same procedure as for the layered samples with a few exceptions. The substrate cleaning step was executed in a similar way, but the microsphere preparation step was omitted. The microspheres were now prepared in step 3, as a part of the preparation of the paint. In this step the ZnO-paint was be doped with microspheres. The preparation of this doped ZnO-paint will be discussed in this subsection. The fabrication of the layer was again executed in the same way as was done for the layered samples.

3. **Doped ZnO-paint preparation**
   The preparation of the ZnO-paint for the dispersed samples deviates from the preparation for the layered samples. The fluorescent microspheres were now added to the ZnO-paint. We started again with ZnO-powder [35] to make a suspension of 8.5 volume percent ZnO in water. The suspension was stirred for 30 minutes and immersed into a ultrasonic bath for 15 minutes. Then $9{\cdot}10^{-4}$ volume percent of the undiluted microsphere suspension was added to the ZnO-paint. Again the suspension was stirred thoroughly for 30 minutes and it was placed in the ultrasonic bath for 15 seconds.

4.3 Sample characterization

It is important that our samples are thick enough to fully scatter all the incoming light so that they are opaque. The average distance light can propagate inside the sample before it is being scattered is defined by the transport mean free path, ℓ_{tr}. For the characterization of our samples we want to measure the thickness of our samples and we want to determine ℓ_{tr}.

By measuring the total transmission as a function of the sample thickness, we determined ℓ_{tr}. From diffusion theory (see section 2.3.3) it is found that the total transmission, T, depends on ℓ_{tr}, the thickness of the sample, L, and the extrapolation lengths, z_{e1} and z_{e2}:

$$\frac{1}{T} = \frac{L + z_{\mathrm{e1}} + z_{\mathrm{e2}}}{\ell_{\mathrm{tr}} + z_{\mathrm{e1}}}. \tag{4.1}$$

The extrapolation lengths account for the reflections of the light at the boundaries of the sample [12, 13]. Because one side of the sample has a glass/ZnO boundary while the other side of the ZnO layer abuts on air, the two extrapolation lengths are different. Using calculations on the angular distribution of diffusive transmitted light [37][1] we found a relation between z_1 and z_2 independent of the refractive index of the sample:

$$z_{\mathrm{e2}} = 0.34\ell_{\mathrm{tr}} + 0.87 z_{\mathrm{e1}}. \tag{4.2}$$

The total transmission of the samples was measured using an integrated sphere. In Fig. 4.3 a schematic view of the setup for the total transmission measurements is shown. The samples were placed on top of the integrating sphere. They were illuminated by laser light with a wavelength of $\lambda = 532$ nm. The transmitted light was collected inside the integrating sphere and was scattered multiple times before hitting the detector. Light looses all dependence on the original direction because of multiple scattering inside the integrating sphere. Light that left the sample under different angles is mixed. The intensity detected at the detector is therefore an average over all angles. The baffle prevents light coming from the sample from hitting the detector directly. The transmission intensities are referenced to the transmission intensity of a bare coverglass, which represents a transmission of 100 %. To determine the thickness of the samples, we made a scratch throughout the ZnO layer and then measured the depth of the scratch using a optical microscope[2].

In Fig. 4.4 the inverse relative total transmission is plotted against the thickness of the sample. The data is fitted by a linear function. From the slope of the fit and the intercept with the y-axis at $L = 0\ \mu$m, we determined l_{tr} using Eq. 4.1 and Eq. 4.2. We found ℓ_{tr} to be $0.72 \pm 18\ \mu$m.

4.4 Conclusions

In this chapter we discussed the fabrication and characterization of the samples that are used in our experiments. We showed how we fabricated two different types of samples. The first type consist of fluorescent microspheres on a glass substrate, covered by a scattering

[1] A Mathcad® program was used to perform the calculations. The program was originally written by Drs. D.H. Dau and later modified by Dr. B. Bret.

[2] Both the thickness and the total transmission measurements were performed by Ir. I.M. Vellekoop.

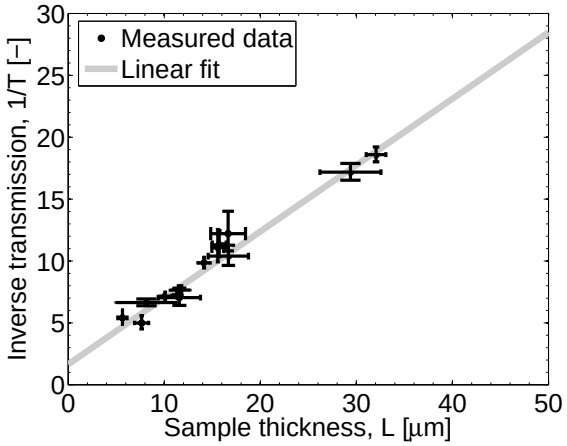

Figure 4.4: Inverse total transmission versus the sample thickness. The total transmission is referenced to the transmission of a bare coverglass. The solid line is a linear fit to the data points. This fit yields $\ell_{tr} = 0.72 \pm 18\,\mu$m.

layer of ZnO pigment. The second type consist out of a scattering layer of ZnO pigment on a glass substrate, with fluorescent microspheres dispersed throughout the scattering layer. For both types of samples we used an airbrush to spray the ZnO onto the glass substrates.

Our fabrication procedure has proven to be successful and easily reproducible. The scattering layers of our samples were found to between 6 and 32 μm thick. The samples were fully opaque and the transport mean free path was measured to be $0.72 \pm 18\,\mu$m. Due to the absence of a suitable binder, we had to suspend our ZnO pigment in water. Therefore the surface of the samples is not smooth and flat but is found to be granular and curved. The absence of a binder also makes the samples fragile.

The fluorescent microspheres are well hidden deeply inside or under the opaque layer and are not discernable with standard microscope techniques.

CHAPTER 5

Experimental Results

5.1 Introduction

We performed different experiments where we focussed light on a target position deeply inside a strongly scattering sample using a channel demixing technique. Incident light entering through scattering channels is mixed due to the scattering inside the sample. This mixing of channels results in a granular intensity pattern throughout the whole sample. With the channel demixing technique we introduce different phase shifts for the independent channels, such that the channels demix at a certain target position inside the opaque sample. While standard wavefront correction techniques break down when light is scattered a few times, we succeeded to bring light effectively at targets deeply inside strongly scattering samples. Efficient light delivery at depths of even more than 14 times the transport mean free path ℓ_{tr} was achieved.

In this chapter we present the experimental results of the channel demixing experiments. The experiments were performed for targets at different depths inside the samples. We address the analysis of the data and discuss the different experimental aspects that were needed to determine the achieved intensity enhancements. A comparison is made between standard scanning illumination and the channel demixing technique. Furthermore we present the results of different characterization experiments.

5.2 Channel demixing for probes at different depths[1]

In the channel demixing experiments, we used a spatial light modulator (SLM) to shape the wavefront of a light beam. This light beam was focussed onto a opaque scattering sample

[1] Results presented in Section 5.2 are published as "*Demixing light paths inside disordered metamaterials*" by I.M. Vellekoop, E.G. van Putten, A. Lagendijk and A.P. Mosk [38].

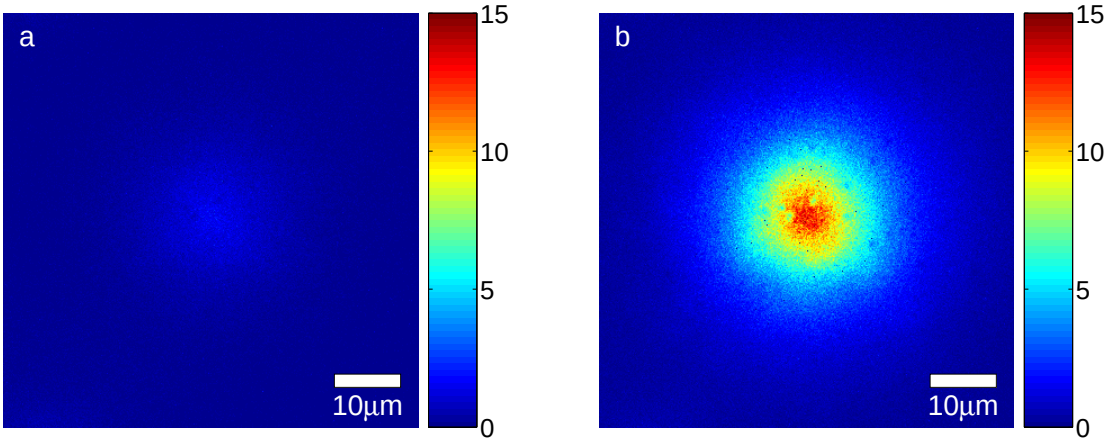

Figure 5.1: Both images show a diffusive spot of fluorescent light, coming from a sphere embedded inside a layer of zinc oxide. In (a) a gaussian wave is focussed onto the opaque sample causing a weak fluorescent response of the embedded sphere. In (b) the opaque sample is illuminated with a shaped wavefront, constructed to optimize the intensity at the position of the sphere. The increased intensity of excitation light inside the sphere results in a considerable brighter fluorescent spot. The intensities are in counts/milliseconds.

with 300 nm fluorescent spheres embedded into it. The shaped wave causes different phase delays for the light entering the sample through different scattering channels. Scattered light, traveling along different paths, interfered constructively at a certain target sphere inside the strongly scattering samples. In Fig. 5.1 we show two images of fluorescent light emitted by a sphere embedded in a layer of zinc oxide. The sample is positioned to maximize the fluorescence intensity using standard illumination. In the left image, a gaussian wave is focussed onto the sample, resulting in a weak fluorescent signal. The right image shows the same sample at the same position, now illuminated with a wavefront shaped to optimize the intensity at the position of the probe. Scattering inside the sample converges the light to the sphere, enhancing the intensity at this position by a factor 18. Because of the increase of excitation intensity inside the sphere, the fluorescent response also intensifies, resulting in the bright fluorescent spot.

Channel demixing experiments were performed on probes located at different depths inside the opaque samples. The experiments were performed on the dispersed samples, where the probes were located inside the scattering layer of the sample. We constructed a wavefront composed out of 640 independent segments, which means that we control 640 independent scattering channels. This wavefront optimized the fluorescent emission from the probe. We determined the depth of the probe from the size of the fluorescent spot at the surface of the sample [39].

In Fig. 5.2 the fluorescent intensities are plotted as function of the depth of the probe. The intensities are referenced to the speckle averaged intensity. The gray diamonds represent the maximum achievable intensity enhancement using standard illumination. An increase of 3.0 ± 0.4 over the reference intensity is found. The black circles show the fluorescence intensity when the sample is illuminated with a shaped wavefront that demixes the channels. This is 18 ± 2.5 times the reference intensity. The intensity enhancement

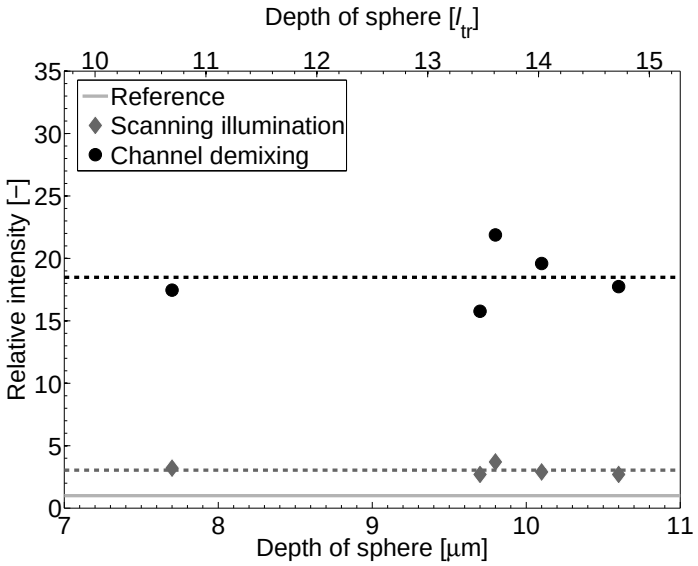

Figure 5.2: Intensities referenced to the speckle average intensity for probes at different depths. We shape the incident wavefront to optimize the amount of light at the position of our probe. As a result we achieve an intensity enhancement of 18 ± 2.5 (black circles). This enhancement is a factor 6 higher than the maximal enhancement possible using standard illumination (grey diamonds), equal to 3.0 ± 0.4. The intensity enhancements seem independent of the depth of the probes.

seems independent of the depth of the probe. Compared to the maximum achievable intensity using standard illumination, we get 6 times more light at the position of our probe. From these results we conclude that light is being focussed inside the medium at the position of the probe.

5.3 Reference measurements

In order to quantify the increase in emission intensity from our fluorescent probe, I_{fl}, we have to define a reference intensity. Two different reference intensities have been defined. The first reference intensity, explained in section 5.3.1, is based on the speckle averaged intensity. The speckle averaged intensity is the expected intensity when the sample is placed at a random position with respect to the incoming beam. The second reference intensity is the maximum achievable intensity possible using standard illumination; that is, we focus a gaussian wave onto the sample and scan the sample with respect to the microscope objective to find the optimal intensity. Comparison with this reference intensity shows immediately the improvement of our method of channel demixing above conventional optics. Section 5.3.2 deals with the details of this reference measurement.

5.3.1 Speckle averaged intensity

Due to scattering, a volume speckle field is formed inside the sample as we illuminate it. The intensity fluctuates at a length scale of $\lambda/2$. Because this speckle pattern depends on the position of the scatterers with respect to the incident light, a small movement of the

sample leads to intensity fluctuations throughout the sample. When the sample is placed at a certain position, it is not obvious whether the fluorescent probe is initially illuminated by a bright or a dark volume speckle, making some kind of averaging necessary.

Aside from the dependence on the position of the scatterers and the position of the incoming beam, the speckle pattern also depends on the shape of the incoming wavefront. If the incoming wavefront is constantly adjusted in a random way, the excitation intensity also fluctuates randomly around some mean value. We find the mean fluorescence intensity within 5% by averaging the recorded fluorescence intensity, I_{fl}, over 500 randomly shaped incoming wavefront. This mean intensity is used as the speckle averaged intensity, I_{ref}.

5.3.2 Scanning illumination

If a gaussian wave is focussed onto an opaque sample, only a negligible part of the incoming light remains unscattered and is focussed at the geometric focus. Moving the sample with respect to the beam only changes the volume speckle pattern. The fluorescence intensity from the probe, I_{fl}, is maximized if the probe is placed inside the brightest volume speckle. If, on the contrary, a scattering sample is thin, the maximal fluorescence intensity is found when the probe is placed in the geometric focus.

We find the position of maximum fluorescent intensity by scanning the sample in three dimensions with respect to the microscope objective. By scanning the sample in the z-direction, perpendicular to the surface, we move the geometric focus of our beam through the whole thickness of the sample with steps of 200 nm. At each depth, z, we scan in a plane parallel to the surface a small range of 1.5 μm with steps of 160 nm around the center of our fluorescent diffusive spot. The steps we take are smaller than $\lambda/2$ to resolve the distinct volume speckles. If there is any unscattered light left we should find a peak in I_{fl} when we scan our probe through the geometric focus.

In Fig. 5.3 we plotted the highest fluorescent intensities at different depths. No intensity peak is seen when the geometric focus is on the same depth of the probe, proving that our samples are thick enough to neglect an unscattered contribution of the light. Figure 5.3 also shows that highest fluorescence intensity value, I_{scan}, is found when the gaussian wave is focussed in the vicinity of the surface of the sample as expected from diffusion theory. If we compare the highest fluorescence intensity, I_{scan}, with the speckle averaged intensity, I_{ref}, we find an intensity enhancement, η_{scan}, of 3.0 ± 0.4. By looking at the statistical intensity distribution inside the sample it is likely to find a speckle with this enhancement factor inside the scanned volume.

During our experiments, we locate the position of the sample at which the probe emits the highest fluorescence intensity, I_{fl} and move our sample to that place subsequent to the construction of our matching wavefront. Repositioning our sample increases the signal to noise ratio. Furthermore it allows us to make a direct comparison of the intensity enhancement we achieve above the highest fluorescence intensity possible using conventional illumination.

5.4 Bleaching and intensity enhancement determination

Our fluorescent probes degenerate during their lifetime. As time progresses, the probes will emit less fluorescent light compared to the amount of excitation light falling on the

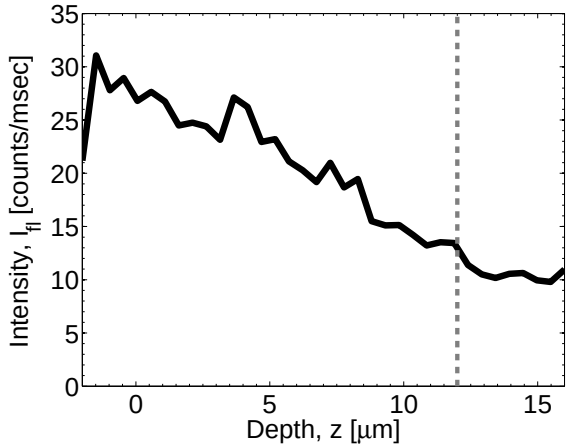

Figure 5.3: Fluorescence intensity versus the depth of the geometric focus. A gaussian wave is focussed onto a sample of zinc oxide containing a fluorescent probe at a depth of 12 ± 0.5 µm. The gray dashed line corresponds to the position of the probe. The maximum fluorescent emission from the probe I_{fl} in the plane parallel to the surface is plotted for different depths of the geometrical focus. The position of the probe was derived from the size of the diffusive fluorescent spot seen at the surface of the sample.

spheres. This process is called photobleaching and is caused by photon-induced chemical damage to the molecules inside the spheres [40]. As the excitation intensity increases, the bleach process of the fluorescent spheres accelerates. The typical timescales belonging to photobleaching are in the order of minutes.

The relation between the absorbed excitation light, I_{ex}, and the emitted fluorescence intensity, I_{fl}, can be approximated in the following way:

$$I_{fl} \propto I_{ex} e^{-\frac{t}{\tau(I_{ex})}}, \tag{5.1}$$

where τ is a time constant proportional to $\frac{1}{I_{ex}}$.

During our experiments the fluorescent probe inside the sample was constantly illuminated by excitation light. Substantial bleaching of the probe was inevitable because the construction of the wavefront takes around 15 to 20 minutes. Figure 5.4 shows a typical fluorescence intensity decay during our optimization experiments where we constructed a optimal wavefront. In the first part of the plot, from $t = 0$ to 18 minutes, the optimal phase shift of each segment was determined. During this optimization we were sending in a almost gaussian wavefront (with exception of the segment which was being optimized). Subsequently the new optimized wavefront was placed on the SLM leading to the large enhancement of I_{fl}. The new wavefront was held steady on the SLM and the decay of I_{fl} is monitored for several minutes. This decay is depicted in the second part of the plot from $t = 18$ to 35 minutes.

When the optimized wavefront is applied to the SLM, I_{fl} shows a large increase. Bleaching of the probe prevents us to make a direct comparison between the enhanced intensity right after the jump, I_{opt}, and the speckle averaged reference intensity, I_{ref}, which was measured before the wavefront construction. A comparison which can be made directly is the enhancement by scanning the sample and the enhancement using an optimized wave-

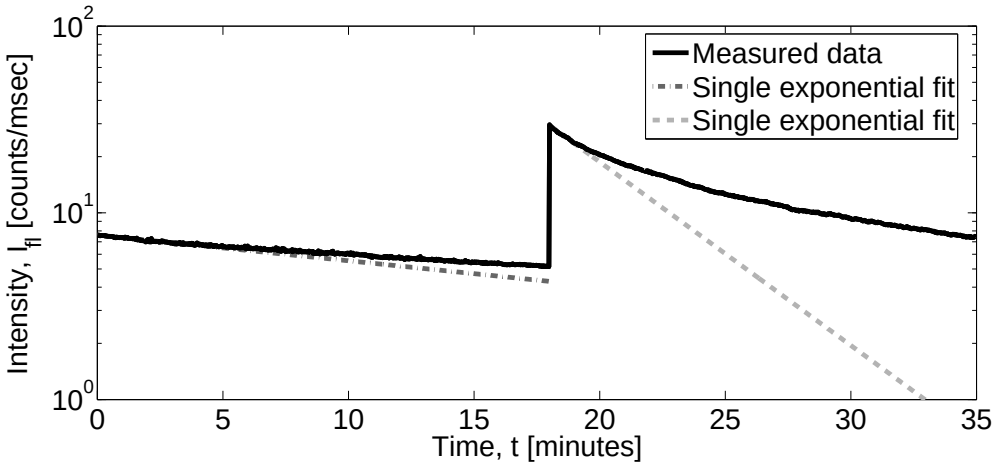

Figure 5.4: Typical intensity decay due to bleaching during the construction of a wavefront. In the first part of the plot, from $t = 0$ to 18 minutes, the optimal phase shifts for each segment is measured. Subsequently these optimized values were set on the SLM and held steady during the second part of the plot, from $t = 18$ to 35 minutes. The first single exponential fit is fitted to the first 40 seconds of the first decay curve and has a time constant of $\tau = 27.6$ mionutes. The second single exponential fit is fitted to the first 40 seconds of the second decay curve and has a time constant of $\tau = 3.9$ minutes.

front, $\frac{\eta_{\text{opt}}}{\eta_{\text{scan}}}$. This enhancement is equal to the intensity jump in Fig. 5.4. Bleaching can be neglected here, because we compare intensities which are recorded right after each other. By comparing the highest fluorescence intensity acquired by scanning the sample with the reference measurement, we determine η_{scan}, and indirectly η_{opt}.

5.5 Stability of the setup

The method explained in the previous section to determine the intensity enhancements, η_{opt} and $\frac{\eta_{\text{opt}}}{\eta_{\text{scan}}}$, is only valid if the displacement of the sample between the beginning and the end of the optimization is negligible; that is, less than $\lambda/2$. Initially the probe in the sample is positioned at a global maximum of excitation light. Each movement of the sample moves the probe away from this maximum leading to a decrease of I_{fl}. The intensity decay in I_{fl} during the optimization could then also be caused by instability. To rule out stability problems we have to ensure that the sample stayed at the same position during the optimization.

We used two different methods to test the stability of the setup during our experiments. In the first method we make use of a two dimensional scan of the sample at the beginning and the end of the experiment. By comparing these two scans with each other the movement of the sample during the experiment can be determined. The second method is based on the bleaching of the probes. The decay curves can be used to extract two independent measures for the intensity increase due to channel demixing. In absence of movement of the sample during the experiment, these two measures should yield the same values.

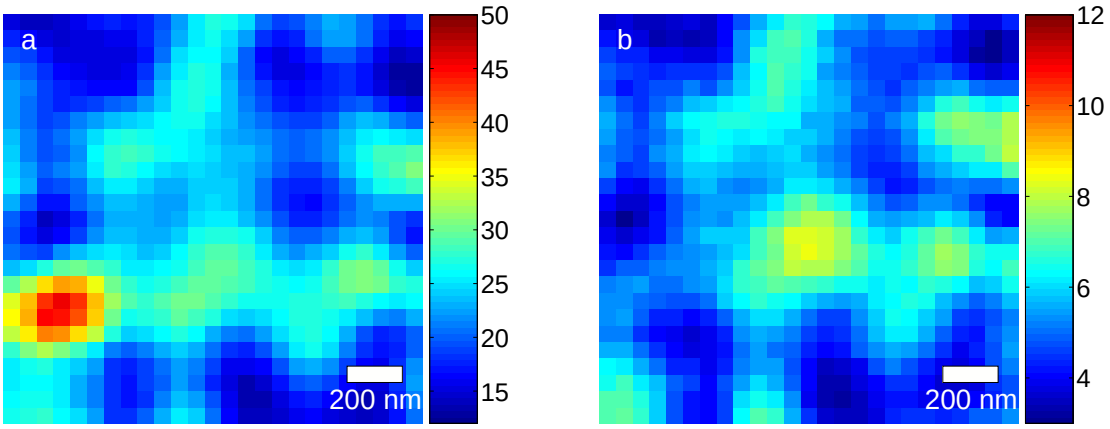

Figure 5.5: Scanning laser micrograph obtained by recording the fluorescence intensity while performing a two dimensional scan of an opaque sample with an embedded fluorescent sphere. The sample is scanned in the plane perpendicular to the incoming beam and is translated in both directions with small steps of 60 nm *over a range of 1.5* μm*. The sample is illuminated with a focussed gaussian wave during both scans. In (a) the results are show of the scan taken at the beginning of the experiment. In (b) the results are show of the scan taken at the end of the experiment. From the distance over which the two patterns are shifted, the displacement of the sample during the experiment can be derived. The intensities are in counts/milliseconds.*

5.5.1 Two dimensional scan of the sample

To test the stability of our sample during the experiments, we perform a two dimensional scan of the sample at the beginning and at the end of each experiment. During these scans, the sample is displaced in the plane perpendicular to the incoming beam and the sample is illuminated with a focussed gaussian wave. The sample is translated in both directions with small steps of 60 nm over a range of 1.5 μm. After each step, the fluorescent emission of the probe is recorded. In this way we map the illumination at the position of the probe as a function of the sample position. If the sample moves during the experiment, this can be seen by comparing the two scans taken in the beginning and the end of the experiment. The two dimensional scans should still show the same pattern but shifted over the same distance as the movement of the sample.

In Fig. 5.5 we show the results of two scans. Figure 5.5 **(a)** was taken at the beginning and Fig. 5.5 **(b)** at the end of the experiment. Comparison of both scans yield the movement of the sample during the experiment. In both images we can recognize the same pattern but shifted over 153 nm. This shift implies that the sample moved over 153 nm during the experiment. In **(a)** we can clearly see that there is one place where the probe emission is higher than for the other sample positions. This position corresponds to the highest speckle spot and the sample is placed at this position during the construction of the wavefront.

It is surprising to see that the large fluorescent emission, seen in the first scan, is completely absent in the scan taken at the end of the experiment. The probe now hardly emits any light when it is placed at the position where the emission intensity was maximum at the beginning of the experiment. During the wavefront construction the sample is placed

onto the position where we found the maximum fluorescent emission. Only a part of the probe is illuminated by one speckle because the size of the probe is larger than the typical size of one speckle. As a consequence, the probe will not bleach homogenously but the illuminated part will bleach faster. The part of the probe which is illuminated the most will dominantly contribute to the total fluorescent emission. The constructed wavefront, based on the measurements of the total fluorescent emission, will therefore focus light onto this already illuminated part of the probe making it bleach even faster. This inhomogeneous bleaching of the probe explains why the large fluorescent emission is absent at the end of the experiment.

5.5.2 Bleaching to test stability

Using the single exponential decay approximation of the bleaching process, as given by Eq. 5.1, we have to two independent ways to determine the intensity increase. The first way uses the intensity jump in I_{fl} at the end of the optimization. This intensity jump should be proportional to the increase in excitation intensity I_{ex}. Using this method we find the intensity increase with and without optimized wavefront both measured at the end of the optimization.

The second method makes use of the difference in decay times, τ, of I_{fl} between the case where the original gaussian wavefront is used and the case where the optimized wavefront is applied. These decay times are proportional to the inverse of the excitation intensity, I_{ex}. We acquire the decay times by fitting a single exponential function to the first 40 seconds of the decay curves. This method gives us the intensity increase without the optimized wavefront at the beginning of the optimization, and with optimized wavefront at the end of the optimization. This determination of the intensity enhancement is not dependent on the bleaching of the probe during the optimization. If the sample did not move during the experiment both methods should give the same value.

5.6 Optimization for different numbers of segments

The maximal enhancement which can be achieved is highly dependent on the number of segments on the SLM that are used to shape the wavefront. We measured the intensity enhancement referenced to the speckle averaged intensity, η_{opt}, as a function of the number of segments that build up the shaped wavefront, N. The number of controlled segments corresponds to the number of controlled scattering channels. The results are plotted in Fig. 5.6.

The measured intensity enhancement η_{opt} is compared with the model from section 2.5.3. For the spheres with a diameter of 300 ± 15 nm, the three electric dipole modes and the three magnetic dipole modes all contribute equally. Higher order (quadrupole) modes do not contribute, so we estimate that there exists $M = 6$ different optical modes inside the volume of the probe. The achieved intensity enhancements show a clear deviation from the model. Especially the enhancement at a larger number of segments lags substantially behind compared to the predicted values of the model. A possible explanation for this discrepancy is the bleaching of the fluorescent probe during the construction of the wavefront and the stability of the sample. Bleaching of the probe degrades the signal

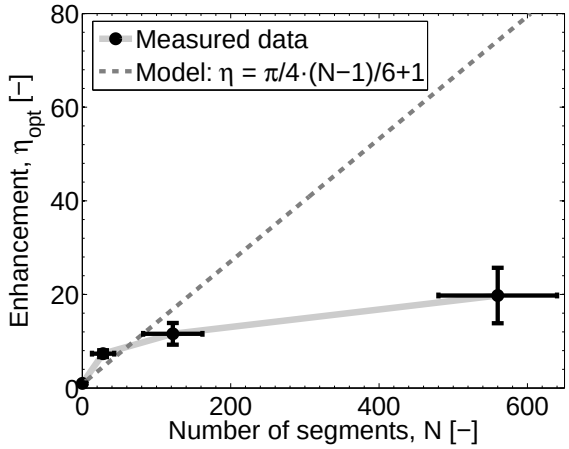

Figure 5.6: The achieved intensity enhancement for wavefronts composed of different numbers of independent segments. The measurements are compared to the theoretical model derived in section 2.5.3 for 6 modes.

to noise ratio. With an increasing number of segments the time needed to construct the wavefront also rises. All this time, the probe is illuminated and bleaches, reducing the signal to noise ratio over time.

The probe is not illuminated homogeneously because the volume of the probe is larger than the typical size of one volume speckle. Different parts of the probe are illuminated differently and do not contribute equally to the total fluorescent emission of the probe. The part of the probe which is initially illuminated the the most by the excitation light, dominates the fluorescent emission and therefore also the construction of the wavefront; the optimization algorithm initially tries to enhance the intensity at this part of the probe. With increasing intensity, the bleaching also increases. As a result, different parts of the probe are bleaching differently. The part where the algorithm is optimizing the light onto, is deteriorating faster than the rest of the probe. After some time, contributions of other parts of the probe to the total fluorescent emission are becoming more and more important. The optimization algorithm now also tries to focus lights at these other parts of the probe, declining the intensity at the original target. This competition decreases the eventual intensity enhancement and could restrain the system to achieve the maximum achievable enhancement.

Instability of the sample also decreases the intensity enhancement. If the sample moves more than $\lambda/2$ the new optimal wavefront lost all correlation with the previous optimal wavefront and the enhancement is completely lost. If the sample moves during the construction of the wavefront, part of the shaped wavefront does not contribute constructively and declines the enhancement partially.

5.7 Looking through the glass

Using the layered samples with the fluorescent probes positioned on the glass/zinc oxide boundary, we are able to see the probes directly from the substrate side of the sample. We use these samples as a test to see if the intensity increase of the fluorescent diffusive spot,

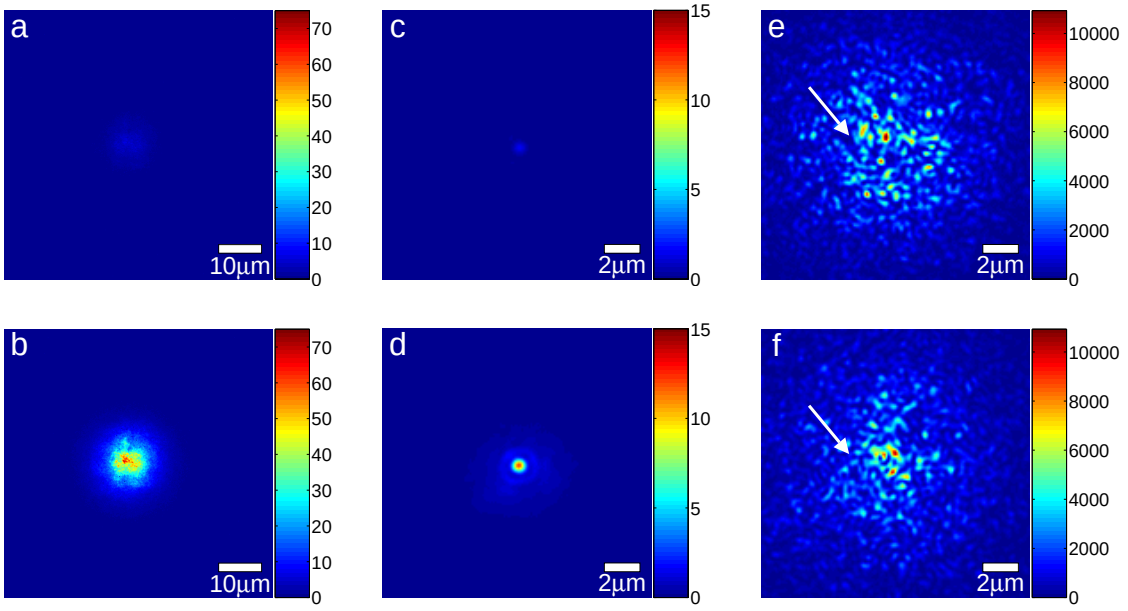

Figure 5.7: Intensity enhancement seen at two different sides of the sample with the probes located at the glass/zinc oxide boundary. We first send in a gaussian wavefront (top row) and then we send in a shaped wavefront which optimizes the fluorescence intensity at the side of the zinc oxide (bottom row). In (a) and (b), the sample is imaged at the zinc oxide side of the sample while the other four figures image the sample from the glass side. Figures (c) and (d) image the fluorescent light, showing a clear image of the probe and (e) and (f) show the green excitation light at the substrate side of the sample. The white arrows indicate the position of the probe.

seen on the side of the zinc oxide, really corresponds to an fluorescence intensity increase of the probe. By looking at the excitation light instead of the fluorescent light, we can see how the speckle pattern changes during the experiment. It is expected that the excitation light shows a bright intensity speckle at the position of the probe.

In Fig. 5.7 we show six images of a layered sample where the probe is located at the glass/zinc oxide boundary. We first send in a gaussian wavefront (top row). Then we send in a shaped wavefront which optimizes the fluorescence intensity at the side of the zinc oxide (bottom row). Figures **(a)** and **(b)** show the fluorescent diffusive spot at the zinc oxide side from the sample and figures **(c)** and **(d)** show the fluorescent probe from the glass side. In figures **(e)** and **(f)** the green excitation light is shown, also at the glass side of the sample. The white arrows point to the position of the probe.

The increase in fluorescence intensity at the side of the zinc oxide, is proportional with the increase of I_{fl} seen at the glass side of the sample. At the position of the probe we also see an increase in excitation light, but this increase is by far not large enough to be consistent with the increase in fluorescence intensity. A possible explanation of this discrepancy lay in the fact that the excitation light propagates through several boundaries before it reaches the camera. At every boundary the light is scattered and the speckle pattern which is recorded by the camera could be totally different from the actual speckle pattern in the plane of the probe. No further investigation has been done to verify this

hypothesis and the cause of this interesting observation remains unclear.

5.8 Conclusions

In this chapter the experimental results of the channel demixing experiments were discussed. Using channel demixing we achieved intensity enhancements of 18 ± 2.5 over the speckle averaged intensity at target positions inside strongly scattering media. Using standard illumination and by performing an exhaustive 3D scan of the sample, we can only get a factor of 3.0 ± 0.4 more light with respect to the speckle averaged intensity. We performed the experiments for probes embedded at different depths inside the scattering samples. We did not found a relation between the depth of the probes and the achieved intensity enhancement. During the experiment the probes bleached substantially which prevented a direct comparison between normal sample illumination and the illumination with the special shaped wavefront. To obtain the correct intensity enhancements at the target positions, we had to correct for the bleaching of the probes.

The volume of the probes is larger than the volume of one optical mode. Therefore we found that probes do not bleach homogenously during the experiments but that the part where we try to optimize the light on bleaches substantially harder than the rest of the probe. As a consequence, the contributions from different parts of the probe to the total fluorescent emission change during the construction of the wavefront. The constructed wavefront will therefore not be the optimal wavefront, limiting the maximal achievable intensity enhancement.

CHAPTER 6

Conclusions

6.1 Conclusions

In this thesis we presented experiments where we focussed light deeply inside opaque scattering samples, proving that it is possible to concentrate light inside an opaque material. Scattering, which is often seen as a detrimental factor, is now used in a beneficial way to deliver light at any desired position. Our method provides a fundamentally new approach to control light inside turbid media.

To achieve a focus inside a strongly scattering sample, we used a technique we call channel demixing. In a scattering sample, the light that enters the sample through different scattering channels is mixed, resulting in a speckle pattern. With the channel demixing technique we controlled the phase of a certain number of incident scattering channels. By applying the right combination of phases, we let the light interfere constructively on a desired target position inside the sample, leading to an intense focus. A fluorescent probe at the target position was used to find the optical combinations of phases and to measure the intensity increase.

The incident light entering through different scattering channels was controlled by a liquid crystal spatial light modulator (LC SLM). This SLM exhibits, like most SLMs, a strong cross-modulation between the phase and the amplitude. We demonstrated a novel modulation technique to achieve full spatial independent control of the phase and the amplitude of the light using a SLM and a spatial filter. With this technique we were able to freely modulate the phase of the light over a range of 2π while keeping the amplitude of the light constant within 2.5%. Furthermore we demonstrated a spatially complex modulation of the light with a high resolution.

All experiments were performed on strongly scattering layers of zinc oxide (ZnO) doped with fluorescent microspheres. Our fabrication procedure, discussed in Chapter 4, has

proven to be successful and easily reproducible. The fully opaque samples had a transport mean free path of $0.7 \pm 0.2\,\mu$m, comparable with the wavelength of light. The fluorescent microspheres were well hidden deeply inside the opaque layer of ZnO and were not discernable with standard microscope techniques.

With channel demixing we achieved intensity enhancements of 18 ± 2.5 times the speckle averaged intensity at different depths inside the opaque sample. The depths were ranging from 8 μm up to 11 μm, corresponding with 11 up to 15 times the transport mean free path of sample. Although the intensity enhancements clearly show that light is focussed inside the opaque sample, we only reach 21% of the theoretical expected intensity enhancement. We believe that the most important reason for not reaching this theoretical maximal value is photo bleaching of the probe. During the construction of the optical phase combinations to focus light inside the opaque sample, the probe bleaches substantially, affecting the maximal achievable enhancement.

We clearly demonstrated that it is possible to concentrate light deep inside opaque materials. Scattering is no longer an unbreakable barrier in, for example, imaging or communication, opening the way for a large range of exciting new applications and advanced research techniques.

6.2 Suggestions for improvement

During our experiments, we found that the fluorescent probes bleached significantly. This bleaching limited us in the achievable intensity enhancement. We expect that with the use of more stable probes we are able to achieve even higher intensity ratios, closer or equal to the theoretical maximum intensity. One can think of quantum dots or spheres doped with more stable fluorescent dyes.

Furthermore a reduction of the probe size will increase the theoretical maximum intensity. Smaller probes support fewer optical modes, and it is therefore possible to focus light more effectively. Doped polystyrene nanospheres with a diameter of 160 nm should in theory only support three electric field modes; one for each polarization. These spheres are commercially available and can be used for further channel demixing experiments.

The turbid samples we use in our channel demixing experiments, should be stable on a timescale of one optimization. Biological tissue is moving to fast to construct a optimal phase pattern using our current liquid crystal spatial light modulator (LC SLM). The time required for achieving a focus should be reduced to below 1 ms per segment [41] to make channel demixing suitable for biological tissue. The fastest SLMs on the market nowadays are micromirror devices that can modulate light in 200 μs. These SLMs should in principle be fast enough to achieve an intensity enhancement in biological tissue.

6.3 Outlook

Channel demixing is a new exciting technique, of which the development started only a few years ago by members of our group. The technique is still in its infancy, but we envision a bright future for channel demixing in both basic research and clinical applications.

With channel demixing, we measure a set of complex propagation amplitudes that describe the propagation of light from a sub-wavelength source inside the sample. This set of

complex amplitudes, which was not experimentally accessible before, contains information about the structure and the optical quality of the sample under investigation. Channel demixing is a unique method to characterize your sample.

In biological imaging, scattering of light severely limits the achievable resolution and contrast of images. Efficient light delivery by channel demixing deep inside tissue could help existing imaging techniques, like OCT and fluorescence microscopy, to produce clearer and more detailed images. Another clinical application of channel demixing could be in the field of photodynamic therapy (PDT) [42]. PDT is a valuable clinical tool for the diagnosis and treatment of skin cancers. In PDT, a tumor localizing photosensitizer agent is applied to the patient after which the treating area is illuminated with laser light. When illuminated, the photosensitizer reacts very rapidly with any nearby molecules, killing the cancer cells. The application of PDT now is limited to the treatment of cancers in or right under the skin, because the light cannot penetrate deep enough inside tissue to reach malicious cells that lay deeper inside the body. Channel demixing could be used to deliver the laser light deeper into tissue, making PDT attractive for treatment of other cancers as well.

Bibliography

[1] D. Huang *et al.*, *Optical coherence tomography*, Science **254**, 1178 (1991). — p.18.

[2] B. B. Das, K. M. Yoo, and R. R. Alfano, *Ultrafast time-gated imaging in thick tissues a step toward optical mammography*, Opt Lett **18**, 1092 (1993). — p.18.

[3] R. Cubeddu, P. Taroni, and G. Valentini, *Time-gated maging system for tumor diagnosis*, Optical Engineering **32**, 320 (1993). — p.18.

[4] C. L. Gordon, III *et al.*, *Time-gated imaging with an ultrashort-pulse, laser-produced-plasma x-ray source*, Opt Lett **20**, 1056 (1995). — p.18.

[5] J. K. Foskett and S. Grinstein, *Noninvasive techniques in cell biology* (Wiley-Liss, 1990). — p.18.

[6] I. M. Vellekoop and A. P. Mosk, *Focusing coherent light through opaque strongly scattering media*, Optics Letters **32**, 2309 (2007). — p.18, 31, 32, 36, and 42.

[7] J. F. de Boer, *Optical fluctuations on the transmission and reflection of mesoscopic systems*, Ph.D. thesis, University of Amsterdam, 1995. — p.21, 24, and 28.

[8] M. C. W. van Rossum, *Mesoscopic phenomena in multiple light scattering*, Ph.D. thesis, University of Amsterdam, 1995. — p.21.

[9] M. C. W. van Rossum and T. M. Nieuwenhuizen, *Multiple scattering of classical waves*, Rev. Mod. Phys. **71**, 313 (1999). — p.21.

[10] I. M. Vellekoop, *Time Resolved Measurements on Diffusion of Light*, Master's thesis, University of Twente, 2003. — p.21, 22, 23, and 24.

[11] B. Bret, *Multiple light scattering in porous gallium phosphide*, Ph.D. thesis, University of Twente, 2005. — p.21 and 45.

[12] A. Lagendijk, R. Vreeker, and P. de Vries, *Influence of internal reflection on diffusive transport in strongly scattering media*, Phys Lett A **136**, 81 (1989). — p.26 and 49.

[13] J. X. Zhu, D. J. Pine, and D. A. Weitz, *Internal reflection of diffusive light in random media*, Phys. Rev. A **44**, 3948 (1991). — p.26 and 49.

[14] C. W. J. Beenakker, *Random-matrix theory of quantum transport*, Rev. Mod. Phys. **69**, 731 (1997). — p.28.

[15] J. W. Goodman, *Speckle phenomena in optics* (Roberts & Company, Englewood, 2006). — p.28, 29, and 31.

[16] E. G. van Putten, I. M. Vellekoop, and A. P. Mosk, *Spatial amplitude and phase modulation using commercial twisted nematic LCDs*, ArXiv.org:physics.optics/0711.4301 (2007). — p.35.

[17] J. F. Le Gargasson, M. Glanc, and P. Léna, *Retinal imaging with adaptive optics*, C. R. Acad. Sci. Paris. Series IV **2**, 1131 (2001). — p.36.

[18] J. M. Beckers, *Adaptive optics for astronomy - Principles, performance, and applications*, Annual review of astronomy and astrophysics **31**, 13 (1993). — p.36.

[19] D. Psaltis and G. Burr, *Holographic data storage*, Computer **31**, 52 (1998). — p.36.

[20] A. R. L. Travis, *The display of three-dimensional video images*, Proceedings of the IEEE **85**, 1817 (1997). — p.36.

[21] J. A. Davis, D. E. McNamara, and D. M. Cottrell, *Encoding complex diffractive optical elements onto a phase-only liquid-crystal spatial light modulator*, Optical Engineering **40**, 327 (2001). — p.36.

[22] T.-L. Kelly and J. Munch, *Phase-Aberration Correction with Dual Liquid-Crystal Spatial Light Modulators*, Appl. Opt. **37**, 5184 (1998). — p.36.

[23] L. G. Neto, D. Roberge, and Y. Sheng, *Full-range, continuous, complex modulation by the use of two coupled-mode liquid-crystal televisions*, Appl. Opt. **35**, 4567 (1996). — p.36.

[24] R. Dou and M. K. Giles, *Phase measurement and compensation of a wave front using a twisted nematic liquid-crystal television*, Appl. Opt. **35**, 3647 (1996). — p.36.

[25] S. Chavali, P. M. Birch, R. Young, and C. Chatwin, *Synthesis and reconstruction of computer generated holograms by a double pass technique on a twisted nematic-based liquid crystal spatial light modulator*, Optics and Lasers in Engineering **45**, 413 (2007). — p.36.

[26] V. Bagnoud and J. D. Zuegel, *Independent phase and amplitude control of a laser beam by use of a single-phase-only spatial light modulator*, Optics Letters **29**, 295 (2004). — p.36.

[27] V. Arrizón, *Complex modulation with a twisted-nematic liquid-crystal spatial light modulator:double-pixel approach*, Optics Letters **28**, 1359 (2003). — p.36.

[28] P. Birch, R. Young, D. Budgett, and C. Chatwin, *Two-pixel computer-generated hologram with a zero-twist nematic liquid-crystal spatial light modulator*, Optics Letters **25**, 1013 (2000). — p.36.

[29] Z. Zhang, G. Lu, and F. T. S. Yu, *Simple method for measuring phase modulation in liquid crystal televisions*, Optical Engineering **33**, 3018 (1994). — p.37.

[30] I. M. Vellekoop and A. P. Mosk, *Algorithms for inverting diffusion of light in turbid materials*, (unpublished). — p.42.

[31] D. Wiersma, P. Bartolini, A. Lagendijk, and R. Righini, *Localization of light in a disordered medium*, Nature **390**, 671 (1997). — p.45.

[32] R. H. J. Kop, P. de Vries, R. Sprik, and A. Lagendijk, *Observation of Anomalous Transport of Strongly Multiple Scattered Light in Thin Disordered Slabs*, Phys. Rev. Lett. **79**, 4369 (1997). — p.45.

[33] G. van Soest, *Experiments on random lasers*, Ph.D. thesis, University of Amsterdam, 2001. — p.45.

[34] *Fluorescent Microsphere Suspension from Duke Scientific Corporation, ø 300* nm*, excitation maximum 542* nm*, emission maximum 612* nm. — p.47.

[35] *Zinc Oxide powder from Aldrich,* $< 1\mu m$*,* 99.9% *ZnO.* — p.47 and 48.

[36] *Evolution Solo Airbrush from Harder & Steenbeck, 0.4 mm needle diameter.* — p.47.

[37] M. U. Vera and D. J. Durian, *Angular distribution of diffusely transmitted light*, Phys. Rev. E **53**, 3215 (1996). — p.49.

[38] I. M. Vellekoop, E. G. van Putten, A. Lagendijk, and A. P. Mosk, *Demixing light paths inside disordered metamaterials*, Optics Express **16**, 67 (2008). — p.51.

[39] P. N. den Outer, T. M. Nieuwenhuizen, and A. Lagendijk, *Location of objects in multiple-scattering media*, J. Opt. Soc. Am. A **10**, 1209 (1993). — p.52.

[40] L. Song, E. J. Hennink, T. Young, and H. J. Tanke, *Photobleaching Kinetics of Fluorescein in Quantitative Fluorescence Microscopy*, Biophysical Journal **68**, 2588 (1995). — p.55.

[41] B. J. Vakoc *et al.*, *Phase-resolved optical frequency domain imaging*, Optics Express **13**, 5483 (2005). — p.64.

[42] T. J. Dougherty *et al.*, *Photodynamic Therapy*, Journal of the National Cancer Institute **90**, 889 (1998). — p.65.